Mapping the twist-angle disorder and Landau levels in magic angle graphene

A. Uri[1†], S. Grover[1†], Y. Cao[2†], J. A. Crosse[3], K. Bagani[1], D. Rodan-Legrain[2], Y. Myasoedov[1], K. Watanabe[4], T. Taniguchi[4], P. Moon[3,5,6], M. Koshino[7], P. Jarillo-Herrero[2]*, and E. Zeldov[1]*

[1]*Department of Condensed Matter Physics, Weizmann Institute of Science, Rehovot 7610001, Israel*

[2]*Department of Physics, Massachusetts Institute of Technology, Cambridge, Massachusetts 02139, USA*

[3]*New York University Shanghai and NYU-ECNU Institute of Physics at NYU Shanghai, Shanghai, China*

[4]*National Institute for Material Science, 1-1 Namiki, Tsukuba, 305-0044, Japan*

[5]*Department of Physics, New York University, New York 10003, USA*

[6]*State Key Laboratory of Precision Spectroscopy, East China Normal University, Shanghai 200062, China*

[7]*Department of Physics, Osaka University, Toyonaka, 560-0043, Japan*

[†]equal contribution

*corresponding authors

The recently discovered flat electronic bands and strongly correlated and superconducting phases in magic angle twisted bilayer graphene (MATBG) [1,2] crucially depend on the interlayer twist angle θ. Although control of the global θ of about 0.1° has been demonstrated [1–7], little information is available on the distribution of the local twist angles. Utilizing a scanning nanoSQUID-on-tip [8], we attain tomographic imaging of the Landau levels in the quantum Hall state [9] and map the local θ variations in hBN encapsulated devices with relative precision better than 0.002° and spatial resolution of a few moiré periods. We find a correlation between the degree of θ disorder and the MATBG transport characteristics quality. However, even state-of-the-art devices, exhibiting correlated states, Landau fans, and superconductivity, display significant θ variations of up to 0.1° with substantial gradients and a network of jumps, and may contain areas with no local MATBG behavior, highlighting the importance of percolation physics. The correlated states are found to be particularly fragile with respect to twist-angle disorder. The θ gradients generate large gate-tunable in-plane electric fields, unscreened even in the metallic regions, which drastically alter the quantum Hall state by forming edge channels in the bulk of the sample and may significantly affect the phase diagram of the correlated and superconducting states. We establish θ disorder as a fundamentally new kind of disorder, calling for band structure engineering utilizing twist-angle gradients and gate-tunable built-in planar electric fields for novel correlated phenomena and applications.

Strong electronic correlations arise in twisted bilayer graphene when the low energy bands become exceedingly narrow in the vicinity of the magic angle $\theta_M \approx 1.1°$ (MA) [1–7]. The initial estimates of the bandwidth of these flat bands assumed a rigid and uniform rotation between the two graphene sheets leading to a moiré pattern [10–13]. Recent band structure calculations have shown, however, that twist angle relaxation within a single supercell (~13 nm for $\theta \sim 1.1°$), results in electronic reconstruction that significantly modifies the band structure [14,15]. Since the band structure of the flat bands is determined on a scale of several supercells, similarly to the predicted strong effects of heterostrain [16,17], twist angle gradients should modify the single-particle band structure and induce symmetry breaking, possibly leading to properties that have not been considered so far. Moreover, since correlated phenomena may occur due to electronic interactions on distances larger than the supercell, the twist angle variations may affect the stability of the competing orders, enriching the phase diagram of the correlated states.

Scanning tunneling microscopy studies have shown that the local twist angle can vary substantially between different places in the same sample and have resolved stacking faults and structural defects [18–24]. Large inhomogeneities and extensive networks of stacking faults in bilayer graphene have also been observed by transmission electron microscopy (TEM) [15,25–27]. In this work, we provide high-resolution maps of $\theta(\boldsymbol{r})$ in hBN encapsulated MATBG devices. The results reveal significant twist angle gradients that constitute a new type of disorder that strongly affects both the stability of the correlated phases and the magneto-transport characteristics.

Our samples, fabricated using the tear-and-stack technique [28,29], show characteristic MATBG features [1–7], including superconductivity, correlated insulator states at integer fractions of n_s (four electrons per moiré supercell), and Landau fans, from which a global twist angle $\theta = 1.06^{\circ}$ is derived (device B, Fig. 1b). We derive the local maps of $\theta(\boldsymbol{r})$ by imaging the structure of the Landau levels (LL) throughout the sample. In a conventional quantum Hall (QH) state, alternating compressible and incompressible strips are formed near the sample edges where the Fermi energy ε_F resides correspondingly either within the LLs or in the energy gaps between them. These strips carry counterpropagating nontopological, I^{NT}, and topological, I^T, equilibrium currents respectively, as demonstrated recently in graphene [9]. In MATBG, in contrast, these strips are found surprisingly in the bulk of the sample rather than along the edges (Fig. 1a).

We image these currents by utilizing a superconducting quantum interference device fabricated on the apex of a sharp pipette (SQUID-on-tip, SOT, Fig. 1a) [8,9]. The Pb SOT, with a typical diameter $d \approx 200$ nm, is scanned at a height of $h \approx 30$ nm above the sample surface at $T = 300$ mK in out-of-plane magnetic field, $B_a \approx 1$ T. We apply a small *ac* excitation onto the *dc* backgate voltage V_{bg}, which causes a small *ac* displacement $\boldsymbol{r}_{ac}$ of the position of the I^T strips along the direction of the twist angle gradient, $\nabla\theta(\boldsymbol{r})$ (Fig. 1a). The corresponding *ac* Biot Savart magnetic field B_z^{ac}, is directly proportional to the local current density, eliminating the need for current reconstruction (see Methods). It shows a sharp peak whenever the narrow (~50 nm width) incompressible strips pass under the tip (Fig. 1a and Extended Data Fig. 4), providing very sensitive means for nanoscale imaging of the LLs.

Figure 1d shows a sequence of such B_z^{ac} peaks vs. n_e for device *B*, acquired at a fixed SOT position, in comparison with the corresponding trace of R_{xx} (Fig. 1c), at $B_a = 1.08$ T. The positions and the magnitudes of these peaks provide wealth of information. An incompressible QH strip appears at location $\boldsymbol{r}$ in the sample when the local carrier density $n_e(\boldsymbol{r})$ matches an integer number N of full LLs, $|n_e(\boldsymbol{r})| = gN|B_a|/\phi_0$, where g is the LL degeneracy. Hence the spacing, Δn_e, between adjacent peaks reveals the degeneracy g of the LLs. The height of B_z^{ac} peaks is proportional to $I^T = \sigma_{yx}\Delta\varepsilon_n/e$ ($\sigma_{yx} = \nu e^2/h$ is QH conductance, e – elementary charge, ν – integer filling factor, and h is Planck's constant), and thus reflects the energy gap between the adjacent LLs, $\Delta\varepsilon_n = \varepsilon_{|n|+1} - \varepsilon_{|n|}$ (see Methods).

We start by inspecting high dopings, $|n_e| > n_s$, for which the Fermi level ε_F resides in the dispersive bands (yellow in Fig. 1e). Figure 1f presents a zoom-in on the four lowest LLs in the electron-like (*n*) and hole-like (*p*) dispersive bands for device *A* at $B_a = 1.19$ T. The spacing between neighboring peaks is $\Delta n_e = 1.15\times10^{11}$ cm^{-2} which equals $4B_a/\phi_0$, showing that these LLs are fourfold degenerate ($\phi_0 = h/e$). The spacing between the corresponding *p* and *n* LLs equals $2(n_s(\boldsymbol{r}) + 4N|B_a|/\phi_0)$ as illustrated in Fig. 1f. Since the I^T peaks are very sharp, high-accuracy determination of the local $n_s(\boldsymbol{r})$ and thus of the local twist angle $\theta(\boldsymbol{r}) = a\sqrt{\sqrt{3}n_s(\boldsymbol{r})/8}$ ($a = 0.246$ nm is the graphene lattice constant) is attained with absolute accuracy of $\pm0.005^{\circ}$ and relative accuracy between different locations of $\pm0.0002^{\circ}$ (see Methods). In 2D scanning mode described below, we attain sensitivity of 0.007°/Hz$^{1/2}$ and provide $\theta(\boldsymbol{r})$ maps with relative accuracy better than $\pm0.001^{\circ}$.

Rather than parking at a fixed location, Fig. 2a shows B_z^{ac} in device *A* acquired upon scanning the SOT along the white dashed line in Fig. 3a and sweeping V_{bg}, revealing that the LLs vary strikingly in space forming rich patterns. Moreover, the degeneracy of the higher LLs toggles between 4-fold and 8-fold as a function of position, and a pronounced asymmetry between the LL structure in the *n* and *p* dispersive bands is observed.

As in Fig. 1f, by tracing the spacing between the lower LLs we derive the local $n_s(x) = C(V_{ns}(x) - V_{-ns}(x))/2$, where $V_{ns}(x)$ and $V_{-ns}(x)$ are the backgate voltages corresponding to the local filling of the flat bands $|n_e(x)| = n_s(x)$ (dashed yellow curves in Fig. 2a), and C is the backgate capacitance (see Methods). The attained $n_s(x)$ (Fig. 2b) varies by about 2.4×10^{11} cm^{-2} corresponding to the local variation in $\theta(x)$ of 3.9% from 1.124° to 1.169° over the 2.7 μm long path (Fig. 2c). In addition to the twist-angle disorder, which shifts the *p* and *n* LLs antisymmetrically, we also derive the local charge disorder $n_d(x)$, which shifts all the LLs symmetrically through variation of the local charge neutrality point (CNP), $n_d(x) = CV_{CNP}(x) = C(V_{ns}(x) + V_{-ns}(x))/2$. The derived charge disorder $\delta n_d(x) = n_d(x) - \bar{n}_d$ (Fig. 2d) has standard deviation of 0.8×10^{10} cm^{-2} which is substantially smaller than $n_s(x)$ variation, showing that the dominant source of disorder in this MATBG device arises from $\theta(\boldsymbol{r})$ variations, as evident in Fig. 2a by the antisymmetric bending of the dispersive *p* and *n* LLs.

To derive full maps of the local twist angle $\theta(\boldsymbol{r})$ and charge disorder $\delta n_d(\boldsymbol{r})$, we acquired Supplementary Videos 1 to 4 of $B_z^{ac}(\boldsymbol{r})$ upon incrementing V_{bg} through the bottom of the dispersive bands. Figure 3a displays one frame from Supplementary Video 2 showing a large-area scan of device *A* (dashed rectangle in the AFM inset), while Supplementary Video 1 presents zoomed-in imaging of the central region (dashed rectangle in Fig. 3a). The red stripes reveal incompressible regions carrying I^T while the dark blue mark the compressible areas carrying counterpropagating I^{NT}. As V_{bg} varies, the QH states move and change their shape in an intricate manner. Surprisingly, the quantum Hall edge states are present in the bulk of the sample and do not flow parallel to the sample edges as expected. Moreover, large parts of the sample do not show LLs at all. These are the regions that are either highly disordered or may have a very different twist angle, with θ either close to zero or $\theta > 1.5°$ such that the dispersive bands are reached at V_{bg} outside our range. Thus, the MA physics appears only in a limited central region of the sample and does not fully extend to the edges. Figure 3e shows a larger area B_z^{ac} image of device *B* displaying QH states over most of its area. Supplementary Videos 3 and 4 were acquired in the central part of the Hall-bar structure (dashed rectangle in the AFM inset) probing *p* and *n* dispersive bands respectively.

Using these data we generate 3D tomographic rendering of the LLs throughout the samples (see Methods) that can be inspected interactively [30]. Figure 3d shows a slice of the tomographic data of device *A* (see Supplementary Video 5), revealing the layered structure of incompressible (light blue/red) and compressible (dark blue) QH regions. Strikingly, the LLs display steep slopes and numerous small jumps in the bulk of the sample, revealing that at any value of V_{bg} (horizontal tomographic plane) several different LLs cross ε_F in the bulk of the sample never forming a well-defined single QH state. This observation explains the absence of clear conductance oscillations and quantization in the global R_{xx} data in the dispersive bands in Fig. 1c despite the presence of fully developed LLs observed locally in Fig. 1d.

Applying the procedure of Fig. 1f to the tomographic data, we derive 2D maps of the charge disorder (Fig. 3h, see discussion in Methods) and of the twist angle $\theta(\boldsymbol{r})$ in devices *A* and *B* (Figs. 3b,f). The grey-blue color in Fig. 3b reflects areas where no QH states were detected within the measured span of V_{bg}. These regions correlate with the locations of bubbles (black outlines) as revealed by AFM of device *A* (Fig. 3a inset). The magic angle physics is apparently absent within the bubbles as well as in their

surrounding areas up to 0.5 μm from the bubble edges. The LLs are absent also in additional regions where no particular features were observed in the AFM. The map in Fig. 3b also shows that the MA regions in device *A* do not create a percolation path between the contacts. This is consistent with our transport measurements that do not show fully developed superconductivity, although correlated insulating states are present in this device. In device *B*, in contrast, four-probe transport measurements showed high quality correlated insulator states at multiple integer filling factors, and a zero resistance superconducting state (see Methods) consistent with the observation that the MA area extends over the entire length of the central part of the device and shows a more uniform $\theta(\boldsymbol{r})$ (Fig. 3f).

The MA regions show significant twist-angle disorder (Fig. 3i histogram). The $\theta(\boldsymbol{r})$ spans a range of 0.13° (1.05° to 1.18° with standard deviation 0.025°) in device *A* (Fig. 3b) and 0.10° in device *B* (0.98° to 1.08°, standard deviation 0.022°, Fig. 3f). Moreover, the topography of $\theta(\boldsymbol{r})$ is nontrivial with numerous peaks and valleys, as well as saddle points. Since the LLs in the dispersive band follow the bottom of the band, $n_s = 8\theta^2/(\sqrt{3}a^2)$, the LLs first appear at the minimum of $\theta(\boldsymbol{r})$ landscape, which for device *A* occurs in the lower-right corner (dark brown in Fig. 3b). This behavior is clearly visible in Supplementary Video 1 where arc-like incompressible strips (bright) first appear at this corner and upon increasing $|V_{bg}|$ "climb" the amphitheater-like $\theta(\boldsymbol{r})$ landscape following the equi-$\theta(\boldsymbol{r})$ contours. Similar behavior is observed in other regions with particularly interesting dynamics occurring at the saddle points as described in Methods.

The $\theta(\boldsymbol{r})$ derived in Figs. 3b,f appears to be rather smooth with typical gradients of ~0.05°/μm. Remarkably, Figs. 3c,g presenting the gradient, $|\nabla\theta(\boldsymbol{r})|$, reveal that variations in $\theta(\boldsymbol{r})$ partially occur through a network of small steps of variable sizes reaching 0.01°. The derived pattern strongly resembles the stacking fault networks in bilayer graphene observed by TEM [15,25–27]. These steps cause the stepwise jumps in the LLs visible in the tomographic view in Fig. 3d and Extended Data Figs. 8a,c. This finding implies that the smooth variations in $\theta(\boldsymbol{r})$ are accompanied by occasional small abrupt changes across stacking faults that relax the tensile and shear stress.

The revealed twist-angle disorder and gradients $\nabla\theta(\boldsymbol{r})$ may have significant implications on the phase diagram and transport properties of MATBG. Connecting regions of different θ (Fig. 4a) is akin attaching materials with different work functions (Fig. 4b), resulting in band bending and creation of internal electric fields (Figs. 4c-e). The backgate V_{bg} imposes essentially uniform carrier density, $\bar{n}_e \cong CV_{bg}$. Locations with different $\theta(\boldsymbol{r})$, and hence different density of states (DOS), translate this $\bar{n}_e$ into different chemical potential $\mu(\boldsymbol{r})$. Since at thermal equilibrium the Fermi level has to be uniform, $\varepsilon_F = \mu + qV = 0$, (the last equality reflects the grounding of the device) variations in chemical potential $\mu(\boldsymbol{r})$ impose band bending, i.e. variations in electric potential $V(r) = -\mu(\boldsymbol{r})/q$ ($q = \pm e$ is the carrier charge), and creation of in-plane electric field $E_{\parallel} = -\nabla V$ that cannot be screened. Utilizing the DOS derived from band structure calculations (see Methods), Figs. 4c-e present a self-consistent numerical calculation of $V(x)$, $E(x)$, and $\delta n_e(x) = n_e(x) - \bar{n}_e$ at $B_a = 0$ for the case of linearly varying $\theta(x)$ with $\nabla\theta =$ 0.025°/μm comparable to the measured average gradients in Figs. 3c,g. A significant electric field $E \cong$ 0.4 kV/m is formed in the region of varying $\theta(x)$, while the accompanying charge redistribution remains negligible, $\delta n_e/\bar{n}_e \cong \pm 3\times10^{-5}$. Note that for $V_{bg} = 0$, the twist-angle disorder has essentially no effect ($\Delta\mu(\boldsymbol{r}) = 0$ and $E_{\parallel} = 0$) and its impact grows with increasing $|\bar{n}_e|$.

In presence of magnetic field, the DOS variations induced by $\theta(\boldsymbol{r})$ give rise to gradients in the LL energies ε_n as depicted by the blue lines in Fig. 4f (see Methods). As a result, a highly unusual QH state emerges in which instead of being restricted to the edges, the QH edge states are formed in the bulk creating interlaced compressible and incompressible strips with different integer filling factors (Figs. 4g-i). This

absence of well-defined QH state provides an explanation of the fact that MATBG magnetotransport commonly shows SdH oscillations without displaying full conductance quantization [1–7].

In contrast to the conventional QH, in which the edge states must form closed loops, here they seem to terminate in the bulk upon reaching apparently disordered metallic regions (Supplementary Videos 1-4). Moreover, instead of the usually required constant carrier density in the incompressible regions, in presence of a θ gradient the density varies following the variation in $n_s(\boldsymbol{r})$ (Fig. 4i). The $\nabla\theta(\boldsymbol{r})$ also causes accidental LL crossings (red circle in Fig. 4f) giving rise to occasional eight-fold degenerate LLs in the dispersive bands as observed in Figs. 1d, 2a and Extended Data Fig. 6. Figure 4g also shows large electric fields (~10^5 V/m) formed in the incompressible strips giving rise to very narrow channels of persistent current I^T (Fig. 4h) consistent with the experimental data (Extended Data Fig. 4g). The typical width of ~50 nm of the channels along with the local $|\nabla\theta(\boldsymbol{r})|$ determines the spatial resolution of our $\theta(\boldsymbol{r})$ mapping (see Methods).

Finally, we discuss the rich structure observed in the flat bands in Figs. 1 and 2. In contrast to transport measurements that resolve SdH oscillations at high fields where some of the degeneracies may be lifted, we probe the LLs locally at relatively low fields. The 0th LL at CNP is apparently eight-fold degenerate followed by four-fold degenerate LLs on both sides (Fig. 1d). It has been argued that such degeneracy indicates breaking of C_3 symmetry [31,32], which may in turn be triggered by the observed θ gradients. Figures 1d and 2a show that these LLs are sometimes observed to extend beyond $n_s/4$ on both *p* and *n* sides, while at other locations new irregular LLs seem to emerge for *n* doping above $n_s/4$, as visible in Fig. 1d. The LLs clearly reappear above $n_s/2$ for both dopings, showing degeneracy of 2 (Figs. 2a and Extended Data Fig. 7). We occasionally observe single-fold LLs above $3n_s/4$ for both dopings as seen in Figs. 1d and Extended Data Fig. 7. We also observe that the amplitudes of the I^T peaks, which are proportional to energy gaps $\Delta\varepsilon_n$, emanating from different integer fillings, often follow a smooth envelope. This indicates that the energy gaps between consecutive LL are of similar, rather than alternating, magnitudes, indicating full lifting of a degeneracy. Importantly, Figs. 1d, 2a, and Extended Data Fig. 7 show that LLs near $n_s/4$ and $n_s/2$ are discontinuous and those above $3n_s/4$ appear only at a few locations, indicating the extreme fragility of the correlated states to twist-angle disorder.

The twist-angle disorder is a new type of disorder, which is fundamentally different from the more common kinds due to the fact that it changes the local band structure, induces large unscreened electric fields, and its effect grows with carrier density $|n_e|$, explaining the higher visibility of the Landau fan near CNP in transport. The charge disorder in graphene is commonly characterized by the width of the resistance peak at CNP. This width, however, bears essentially no information on twist-angle disorder. Instead, our results suggest that the twist-angle disorder should be quantified by analyzing the width of the resistive peak at n_s and the visibility of the Landau fans at $|n_e| > n_s$. Our finding that the QH state is profoundly altered by the twist-angle gradients suggests that other correlated phases in MATBG, including magnetism and superconductivity, may also be fundamentally transformed by the twist-angle disorder. The gate-tunable intrinsic in-plane electric fields generated by the twist-angle gradients may also be of practical importance for photovoltaic and thermoelectric applications of atomically thin twisted van der Waals materials.

References

1. Y. Cao, V. Fatemi, A. Demir, S. Fang, S. L. Tomarken, J. Y. Luo, J. D. Sanchez-Yamagishi, K. Watanabe, T. Taniguchi, E. Kaxiras, R. C. Ashoori, and P. Jarillo-Herrero, ''Correlated insulator behaviour at half-filling in magic-angle graphene superlattices'', *Nature* **556**, 80–84 (2018).

2. Y. Cao, V. Fatemi, S. Fang, K. Watanabe, T. Taniguchi, E. Kaxiras, and P. Jarillo-Herrero, ''Unconventional superconductivity in magic-angle graphene superlattices'', *Nature* **556**, 43–50 (2018).

3. M. Yankowitz, S. Chen, H. Polshyn, Y. Zhang, K. Watanabe, T. Taniguchi, D. Graf, A. F. Young, and C. R. Dean, ''Tuning superconductivity in twisted bilayer graphene'', *Science* **363**, 1059–1064 (2019).

4. M. Serlin, C. L. Tschirhart, H. Polshyn, Y. Zhang, J. Zhu, K. Watanabe, T. Taniguchi, L. Balents, and A. F. Young, ''Intrinsic quantized anomalous Hall effect in a moiré heterostructure'', *Science* eaay5533 (2019).

5. A. L. Sharpe, E. J. Fox, A. W. Barnard, J. Finney, K. Watanabe, T. Taniguchi, M. A. Kastner, and D. Goldhaber-Gordon, ''Emergent ferromagnetism near three-quarters filling in twisted bilayer graphene'', *Science* **365**, 605–608 (2019).

6. S. L. Tomarken, Y. Cao, A. Demir, K. Watanabe, T. Taniguchi, P. Jarillo-Herrero, and R. C. Ashoori, ''Electronic Compressibility of Magic-Angle Graphene Superlattices'', *Phys. Rev. Lett.* **123**, (2019).

7. X. Lu, P. Stepanov, W. Yang, M. Xie, M. A. Aamir, I. Das, C. Urgell, K. Watanabe, T. Taniguchi, G. Zhang, A. Bachtold, A. H. MacDonald, and D. K. Efetov, ''Superconductors, orbital magnets and correlated states in magic-angle bilayer graphene'', *Nature* **574**, 653–657 (2019).

8. D. Vasyukov, Y. Anahory, L. Embon, D. Halbertal, J. Cuppens, L. Neeman, A. Finkler, Y. Segev, Y. Myasoedov, M. L. Rappaport, M. E. Huber, and E. Zeldov, ''A scanning superconducting quantum interference device with single electron spin sensitivity'', *Nat. Nanotechnol.* **8**, 639–644 (2013).

9. A. Uri, Y. Kim, K. Bagani, C. K. Lewandowski, S. Grover, N. Auerbach, E. O. Lachman, Y. Myasoedov, T. Taniguchi, K. Watanabe, J. Smet, and E. Zeldov, ''Nanoscale imaging of equilibrium quantum Hall edge currents and of the magnetic monopole response in graphene'', *Nat. Phys.* (2019).

10. E. Suárez Morell, J. D. Correa, P. Vargas, M. Pacheco, and Z. Barticevic, ''Flat bands in slightly twisted bilayer graphene: Tight-binding calculations'', *Phys. Rev. B* **82**, 121407 (2010).

11. R. Bistritzer and A. H. MacDonald, ''Moiré bands in twisted double-layer graphene'', *Proc. Natl. Acad. Sci.* **108**, 12233–12237 (2011).

12. J. M. B. Lopes dos Santos, N. M. R. Peres, and A. H. Castro Neto, ''Continuum model of the twisted graphene bilayer'', *Phys. Rev. B* **86**, 155449 (2012).

13. P. Moon and M. Koshino, ''Optical absorption in twisted bilayer graphene'', *Phys. Rev. B* **87**, 205404 (2013).

14. N. N. T. Nam and M. Koshino, ''Lattice relaxation and energy band modulation in twisted bilayer graphene'', *Phys. Rev. B* **96**, 075311 (2017).

15. H. Yoo, R. Engelke, S. Carr, S. Fang, K. Zhang, P. Cazeaux, S. H. Sung, R. Hovden, A. W. Tsen, T. Taniguchi, K. Watanabe, G.-C. Yi, M. Kim, M. Luskin, E. B. Tadmor, E. Kaxiras, and P. Kim, ''Atomic and electronic reconstruction at the van der Waals interface in twisted bilayer graphene'', *Nat. Mater.* **18**, 448–453 (2019).

16. L. Huder, A. Artaud, T. Le Quang, G. T. de Laissardière, A. G. M. Jansen, G. Lapertot, C. Chapelier, and V. T. Renard, ''Electronic Spectrum of Twisted Graphene Layers under Heterostrain'', *Phys. Rev. Lett.* **120**, 156405 (2018).

17. Z. Bi, N. F. Q. Yuan, and L. Fu, ''Designing flat bands by strain'', *Phys. Rev. B* **100**, (2019).

18. G. Li, A. Luican, J. M. B. Lopes dos Santos, A. H. Castro Neto, A. Reina, J. Kong, and E. Y. Andrei, ''Observation of Van Hove singularities in twisted graphene layers'', *Nat. Phys.* **6**, 109–113 (2010).

19. I. Brihuega, P. Mallet, H. González-Herrero, G. Trambly de Laissardière, M. M. Ugeda, L. Magaud, J. M. Gómez-Rodríguez, F. Ynduráin, and J.-Y. Veuillen, ''Unraveling the Intrinsic and Robust Nature of van Hove Singularities in Twisted Bilayer Graphene by Scanning Tunneling Microscopy and Theoretical Analysis'', *Phys. Rev. Lett.* **109**, 196802 (2012).

20. D. Wong, Y. Wang, J. Jung, S. Pezzini, A. M. DaSilva, H.-Z. Tsai, H. S. Jung, R. Khajeh, Y. Kim, J. Lee, S. Kahn, S. Tollabimazraehno, H. Rasool, K. Watanabe, T. Taniguchi, A. Zettl, S. Adam, A. H. MacDonald, and M. F. Crommie, ''Local spectroscopy of moiré-induced electronic structure in gate-tunable twisted bilayer graphene'', *Phys. Rev. B* **92**, 155409 (2015).

21. Y. Jiang, M. Anđelković, S. P. Milovanović, L. Covaci, X. Lai, Y. Cao, K. Watanabe, T. Taniguchi, F. M. Peeters, A. K. Geim, and E. Y. Andrei, ''Flat Bands in Buckled Graphene Superlattices'', *arXiv:1904.10147* (2019).

22. A. Kerelsky, L. J. McGilly, D. M. Kennes, L. Xian, M. Yankowitz, S. Chen, K. Watanabe, T. Taniguchi, J. Hone, C. Dean, A. Rubio, and A. N. Pasupathy, ''Maximized electron interactions at the magic angle in twisted bilayer graphene'', *Nature* **572**, 95–100 (2019).

23. Y. Choi, J. Kemmer, Y. Peng, A. Thomson, H. Arora, R. Polski, Y. Zhang, H. Ren, J. Alicea, G. Refael, F. von Oppen, K. Watanabe, T. Taniguchi, and S. Nadj-Perge, ''Electronic correlations in twisted bilayer graphene near the magic angle'', *Nat. Phys.* (2019).

24. Y. Xie, B. Lian, B. Jäck, X. Liu, C. L. Chiu, K. Watanabe, T. Taniguchi, B. A. Bernevig, and A. Yazdani, ''Spectroscopic signatures of many-body correlations in magic-angle twisted bilayer graphene'', *Nature* **572**, 101–105 (2019).

25. J. S. Alden, A. W. Tsen, P. Y. Huang, R. Hovden, L. Brown, J. Park, D. A. Muller, and P. L. McEuen, ''Strain solitons and topological defects in bilayer graphene'', *Proc. Natl. Acad. Sci.* **110**, 11256–11260 (2013).

26. J. Lin, W. Fang, W. Zhou, A. R. Lupini, J. C. Idrobo, J. Kong, S. J. Pennycook, and S. T. Pantelides, ''AC/AB Stacking Boundaries in Bilayer Graphene'', *Nano Lett.* **13**, 3262–3268 (2013).

27. B. Butz, C. Dolle, F. Niekiel, K. Weber, D. Waldmann, H. B. Weber, B. Meyer, and E. Spiecker, ''Dislocations in bilayer graphene'', *Nature* **505**, 533–537 (2014).

28. Y. Cao, J. Y. Luo, V. Fatemi, S. Fang, J. D. Sanchez-Yamagishi, K. Watanabe, T. Taniguchi, E. Kaxiras, and P. Jarillo-Herrero, ''Superlattice-Induced Insulating States and Valley-Protected Orbits in Twisted Bilayer Graphene'', *Phys. Rev. Lett.* **117**, 116804 (2016).

29. K. Kim, M. Yankowitz, B. Fallahazad, S. Kang, H. C. P. Movva, S. Huang, S. Larentis, C. M. Corbet, T. Taniguchi, K. Watanabe, S. K. Banerjee, B. J. LeRoy, and E. Tutuc, ''van der Waals Heterostructures with High Accuracy Rotational Alignment'', *Nano Lett.* **16**, 1989–1995 (2016).

30. See www.weizmann.ac.il/condmat/superc/software/matbg.

31. K. Hejazi, C. Liu, and L. Balents, ''Landau levels in twisted bilayer graphene and semiclassical orbits'', *Phys. Rev. B* **100**, (2019).

32. Y. H. Zhang, H. C. Po, and T. Senthil, ''Landau level degeneracy in twisted bilayer graphene: Role of symmetry breaking'', *Phys. Rev. B* **100**, (2019).

Acknowledgments: We thank A. Stern and E. Berg for valuable discussions and M. F. da Silva for constructing the COMSOL simulations. This work was supported by the Sagol WIS-MIT Bridge Program, by the European Research Council (ERC) under the European Union's Horizon 2020 research and innovation program (grant No 785971), by the Israel Science Foundation ISF (grant No 994/19), by the Minerva Foundation with funding from the Federal German Ministry of Education and Research, and by the Leona M. and Harry B. Helmsley Charitable Trust grant 2018PG-ISL006. Y.C., P.J.-H. and E.Z. acknowledge the support of the MISTI (MIT International Science and Technology Initiatives) MIT–Israel Seed Fund. Work at MIT was supported by the National Science Foundation (DMR-1809802), the Center for Integrated Quantum Materials under NSF grant DMR-1231319, and the Gordon and Betty Moore Foundation's EPiQS Initiative through Grant GBMF4541 to P.J.-H. for device fabrication, transport measurements, and data analysis. This work was performed in part at the Harvard University Center for Nanoscale Systems (CNS), a member of the National Nanotechnology Coordinated Infrastructure Network (NNCI), which is supported by the National Science Foundation under NSF ECCS award no. 1541959. D.R.-L acknowledges partial support from Fundaciò Bancaria "la Caixa" (LCF/BQ/AN15/10380011) and from the US Army Research Office grant no. W911NF-17-S-0001. M.K. acknowledges the financial support of JSPS KAKENHI Grant No. JP17K05496. J.A.C and P.M. were supported by Science and Technology Commission of Shanghai Municipality Grant No. 19ZR1436400, NYU-ECNU Institute of Physics at NYU Shanghai, and New York University Global Seed Grants for Collaborative Research. J.A.C. acknowledges support from National Science Foundation of China Grant No. 11750110420. This research was carried out on the High Performance Computing resources at NYU Shanghai. K.W. and T.T. acknowledge support from the Elemental Strategy Initiative conducted by the MEXT, Japan, A3 Foresight by JSPS and the CREST (JPMJCR15F3), JST.

Author contributions: A.U., S.G. and E.Z. designed the experiment. A.U., S.G. and Y.C. performed the measurements. A.U. and S.G. performed the analysis. Y.C., D.R.-L and P.J.-H designed and provided the samples and contributed to the analyses of the results. K.B. fabricated the SOTs. Y.M. fabricated the tuning forks. J.A.C. performed the tight binding calculations with P.M. and M.K., and K.W. and T.T. fabricated the hBN. A.U., S.G. and E.Z. wrote the manuscript. All authors participated in discussions and in writing of the manuscript.

Competing interests: The authors declare no competing interests.

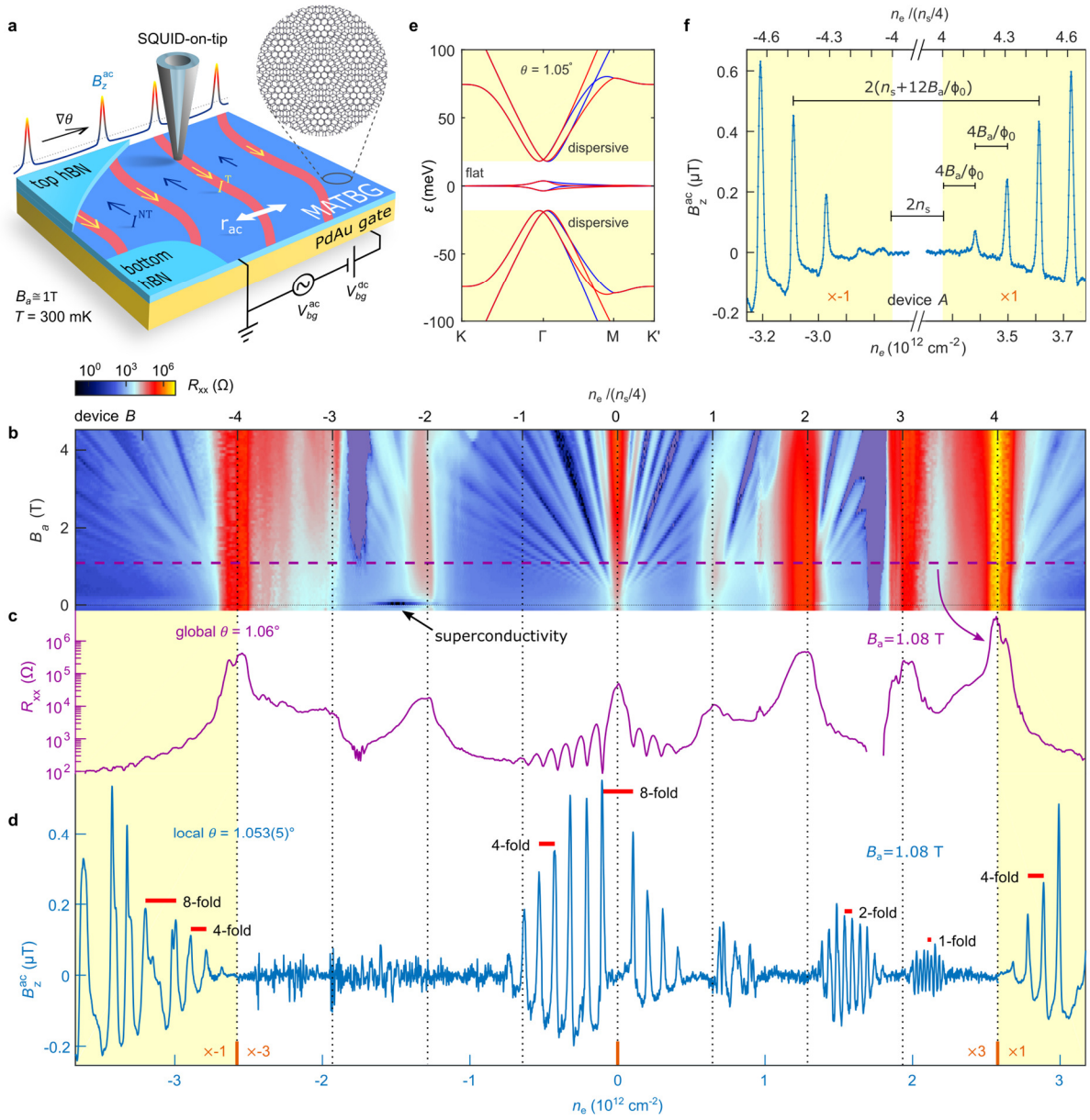

Fig. 1. Comparison between the global and local quantum Hall signatures in flat and dispersive bands in MATBG. (**a**) Experimental setup schematics with SOT scanning over MATBG (blue) encapsulated in hBN (light blue). Voltage $V_{bg}^{dc} + V_{bg}^{ac}$ is applied between the PdAu backgate and the grounded MATBG. Twist angle gradient $\nabla\theta$ induces internal electric field and counterpropagating equilibrium QH topological I^T and nontopological I^{NT} currents in narrow incompressible (red) and wider compressible (blue) strips respectively, flowing along equi-θ contours and detected by B_z^{ac}. (**b**) Global R_{xx} vs. electron density n_e and B_a of device *B* showing insulating states at integer fillings $n_e/(n_s/4)$, Landau fans and superconductivity. (**c**) $R_{xx}(n_e)$ at $B_a = 1.08$ T (extracted from (b) along the dashed purple line). (**d**) B_z^{ac} measured at a point in the bulk of device *B* vs. n_e at $B_a = 1.08$ T. The sharp B_z^{ac} peaks reflect I^T in incompressible strips with sign determined by σ_{yx}, magnitude by LL energy gap, and separation by LL degeneracy (red bars). The dispersive bands are shaded in yellow, the signal in the flat bands is amplified 3 times, and the p-bands signal is multiplied by minus sign for clarity. (**e**) Calculated band structure with flat and dispersive bands. Blue and red represent the two valleys. (**f**) Zoomed-in B_z^{ac} peaks in the dispersive bands for device *A* at $B_a = 1.19$ T, illustrating the procedure for determining the local n_s and the corresponding local θ (*p*-band signal is multiplied by minus sign).

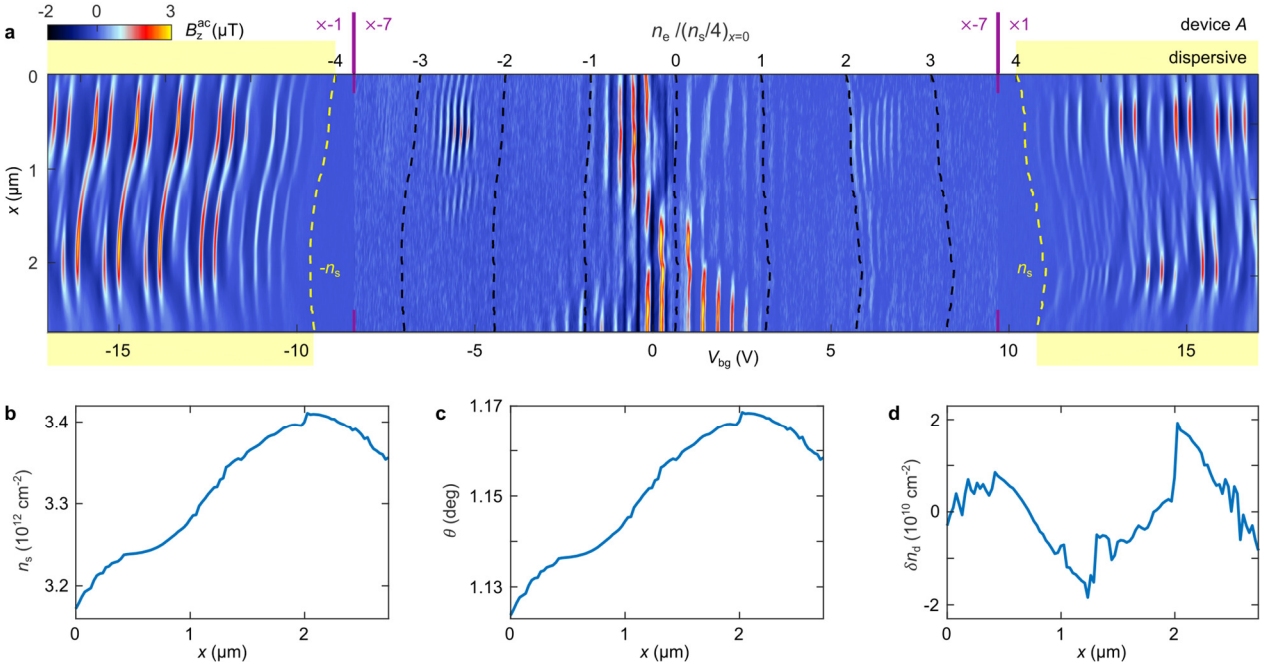

Fig. 2. Structure of the Landau levels and derivation of the twist angle along a line scan. (**a**) $B_z^{ac}(x)$ vs. V_{bg} for device *A* acquired along the dashed line in Fig. 3a. The top axis denotes $n_e/(n_s(x)/4)$ for $x = 0$ and the separation between the yellow dashed lines describes the evolution of $n_s(x)$. The dispersive band regions are marked in yellow. The signal in the flat bands is amplified 7 times and multiplied by minus one for *p*-doping such that incompressible strips are bright. (**b**-**d**) The derived position-dependent $n_s(x)$ (**b**), $\theta(x)$ (**c**), and the charge disorder $\delta n_d(x)$ (**d**).

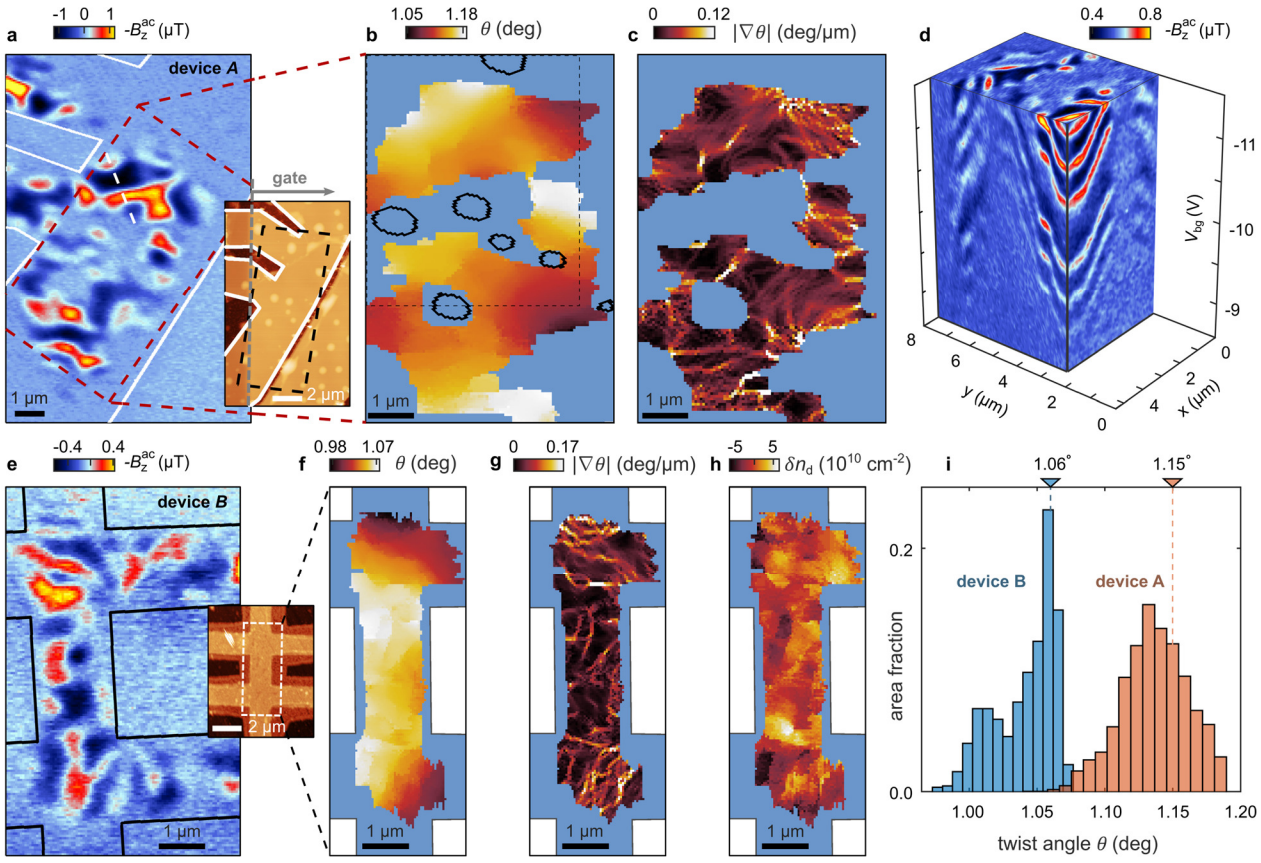

Fig. 3. Mapping the twist angle and Landau levels in MATBG. (**a**) B_z^{ac} image of the dashed area in the AFM inset at $V_{bg} = -16.4$ V. Incompressible (compressible) QH regions are visible as bright blue to yellow (dark blue). Inset: AFM image of hBN encapsulated MATBG device *A* with edges outlined in white, light brown area indicating the underlying PdAu backgate, and bright spots showing bubbles. (**b**) 2D map of the twist angle $\theta(\boldsymbol{r})$ derived from tomography of Supplementary Video 1 in the dashed region in (a). Grey-blue indicates regions which do not display MATBG physics due to disorder (bubbles outlined in black) or due to a very different twist angle. The dashed area is presented tomographically in (d). (**c**) 2D map of $|\nabla\theta(\boldsymbol{r})|$ showing patches of slowly varying $\theta(\boldsymbol{r})$ and a network of abrupt θ jumps. (**d**) Slice from the tomography of device *A* showing disordered LLs in the bulk of the sample in the *p* dispersive band (see Supplementary Video 5 and [30] for interactive interface). The x-axis is flipped for clarity. (**e-g**) Same as (a-c) for device *B* with (e) acquired at $V_{bg} = -15$ V and (f) derived from tomography of Supplementary Videos 3 and 4. (**h**) Charge disorder map $\delta n_d(\boldsymbol{r})$ of device *B*. (**i**) Histogram of local θ in devices *A* and *B* with dashed lines marking the global θ derived from transport.

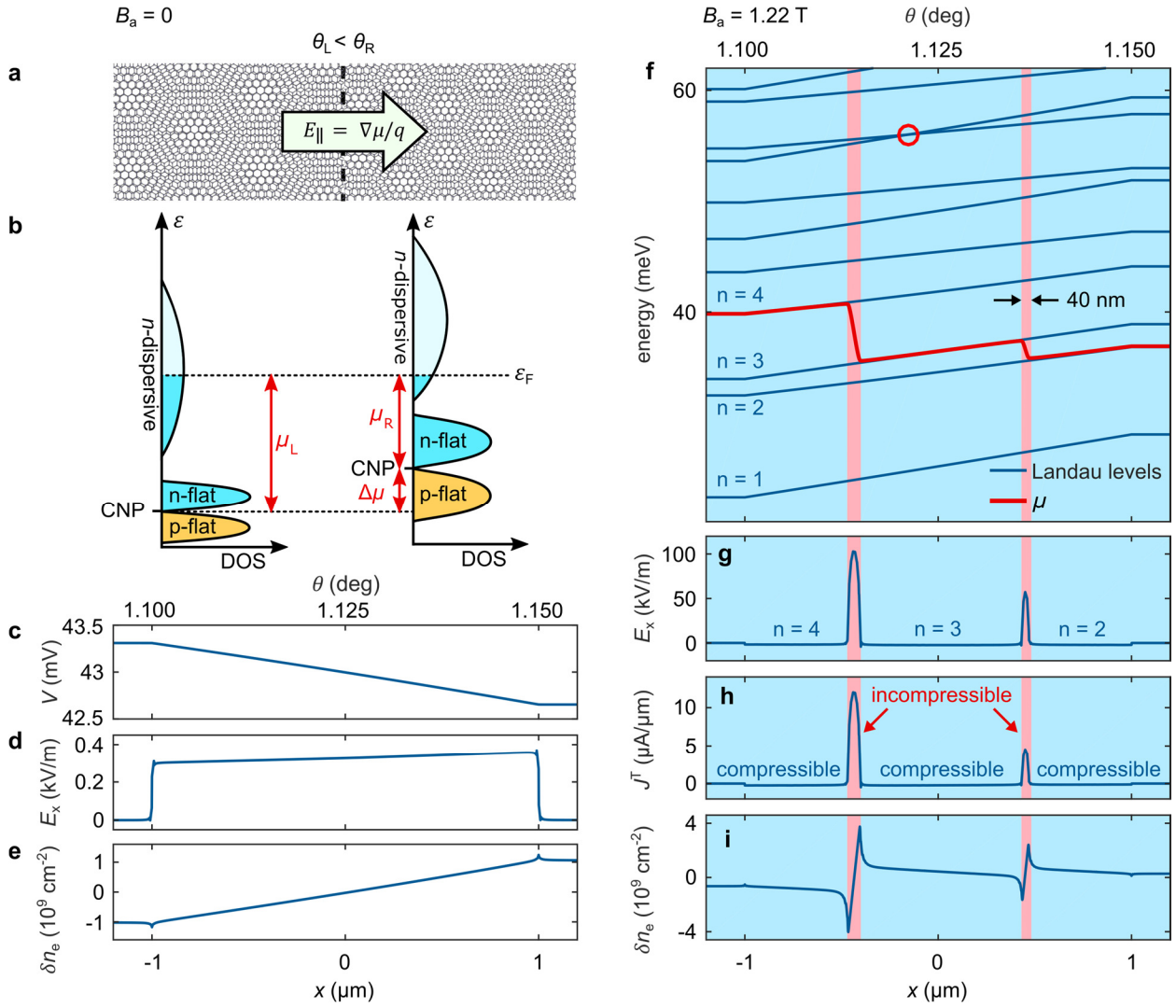

Fig. 4. Internal electric fields, unconventional QH state, and equilibrium currents induced by twist-angle gradients. (**a**) Cartoon of a MATBG sample with two connected regions of different twist angle giving rise to internal electric field $E_\parallel$. (**b**) Schematic DOS in the two regions having different n_s. The backgate voltage V_{bg} imposes nearly the same electron density $\bar{n}_e$ (blue areas) in the two regions, however, the difference in n_s results in different chemical potentials μ_L and μ_R, giving rise to $E_\parallel = \nabla\mu/q$. (**c-e**) Finite element calculation of the potential $V(x) = -\mu(x)/q$ (**c**), electric field $E_x(x)$ (**d**), and carrier concentration $\delta n_e = n_e(x) - \bar{n}_e$ (**e**) for the case of linear change in θ from 1.10° to 1.15° with 0.025°/μm gradient and average carrier density $\bar{n}_e$= 3.25×10^{12} cm^{-2} at $B_a = 0$. (**f-i**) Single particle calculation of LL energies $\varepsilon_n(x)$ in the electron-like dispersive band and self-consistent calculation of chemical potential $\mu(x)$ (**f**), $E_x(x)$ (**g**), $J^T(x)$ (**h**), and $\delta n_e(x)$ (**i**) at $B_a = 1.22$ T. Sharp peaks in E_x and J^T correspond to narrow (~50 nm wide) incompressible strips (shaded red) that are observed experimentally as peaks in B_z^{ac}.

Methods

Device fabrication

The MATBG devices were fabricated using previously reported 'tear & stack' technique [28,29,33]. We first exfoliate monolayer graphene and hBN of 10 to 50 nm thickness on SiO_2/Si substrates, annealed at 350° C (for hBN only) and selected using optical microscopy and atomic force microscopy. Only flakes without wrinkles and bubbles are used. PC/PDMS polymer stack on a glass slide mounted on a micro-positioning stage is used to pick up a ~10 nm thick hBN flake. The edge of the hBN flake is then used to tear a graphene flake. The substrate is rotated by 1.1° to 1.2°, followed by pickup of the other piece of graphene. The resulting stack is encapsulated with another hBN flake of thicknesses of 30 to 70 nm which has been put onto a metallic gate made of evaporated Cr/PdAu. The device geometry is defined by electron-beam lithography and reactive ion etching, only keeping relatively clean regions. Electrical contacts to the MATBG were made by one-dimensional edge contact method [34].

Optical images of devices *A* and *B* are shown in Extended Data Figs. 1a,b respectively. Device *A* was fabricated on a degenerately doped Si substrate with 300 nm SiO_2. The MATBG resides partly on SiO_2 and partly on the evaporated metallic backgate (light brown in Extended Data Fig. 1a). In this work, only the metallic backgate has been used for varying the carrier concentration n_e and a constant voltage $V_{bg}^{Si} =$ 50 V was applied to the Si backgate for keeping the rest of the sample conductive in the transport measurements. Device *B* was fabricated on an intrinsic Si substrate with a metallic backgate extending over the full size of the device (light blue in Extended Data Fig. 1b).

Transport characteristics

Four-probe resistance measurements of the samples at $T = 300$ mK are shown in Extended Data Figs. 2 and 3. Both devices exhibit the common transport characteristics of correlated physics in MATBG [1–3,5–7], including R_{xx} peaks at n_s and its integer fractions, and Landau fans at elevated magnetic field. The slopes of the Landau fans in Extended Data Figs. 2a,b were used to extract the backgate capacitances C of 3.07×10^{11} cm^{-2} V^{-1} (49.23 nF/cm^2) in device *A* and 2.31×10^{11} cm^{-2} V^{-1} (37 nF/cm^2) for device *B* consistent with the evaluated dielectric thickness of the underlying hBN. The origins of the Landau fans were used to derive the global n_s and the corresponding global $\theta = 1.15^{\circ}$ for device *A* and $\theta = 1.06^{\circ}$ in device *B*, in good correspondence with histograms of the local twist angle in Fig. 3i. In device *A* the global θ correlates with the average of $\theta(\boldsymbol{r})$ distribution, whereas in device *B* it is close to the upper end of the distribution function. This is consistent with the fact that the four-probe transport measurements in device *B* probe the central part of the Hall bar structure (Extended Data Fig. 1b) where $\theta(\boldsymbol{r})$ is the highest and significantly more uniform (Fig. 3f), while the low end tail of $\theta(\boldsymbol{r})$ distribution arises from regions that are not probed by transport.

In addition, in device *B* we observe the superconducting state in the vicinity of *p*-doped $n_s/2$ with zero R_{xx} which becomes suppressed by small magnetic field (Extended Data Fig. 3b). The critical current in the superconducting state reaches about 100 nA, as determined by the differential dV/dI characteristics (Extended Data Fig. 3c), and depends sensitively on the carrier density n_e. The observation of a fully developed superconductivity in device *B* is consistent with the finding of a continuous region of MA between the voltage contacts in Fig. 3f. Suppression of the resistance was also observed in device *A* (Extended Data Fig. 3a), but the lowest R_{xx} was 328 Ω, suggestive of the presence of some superconducting regions but absence of a percolation path between the voltage contacts, consistent with the θ map in Fig. 3b.

SOT fabrication and characterization

The Pb SOTs were fabricated as described in Ref. [8] with diameters ranging from 220 to 250 nm and included an integrated shunt resistor on the tip [35]. The SOT readout was carried out using a cryogenic SQUID series array amplifier (SSAA) [36–38]. The magnetic imaging was performed in a ^{3}He system [39] at 300 mK at which the Pb SOTs can operate in magnetic fields of up to 1.8 T. At fields $B_a \approx 1.2$ T used in this study, the SOTs displayed flux noise down to 250 nΦ_0/Hz$^{1/2}$, spin noise of 10 μ_B/Hz$^{1/2}$, and field noise down to 10 nT/Hz$^{1/2}$. For height control we attached the SOT to a quartz tuning fork as described in Ref. [40]. The tuning fork was electrically excited at the resonance frequency of ~33 kHz. The current through it was amplified using a room temperature home-built trans-impedance amplifier, designed based on Ref. [41] and measured using a lock-in amplifier. The scanning was performed at a constant height of 20 to 100 nm above the top hBN surface.

Direct current imaging technique and evaluation of the current in the incompressible strips

In order to avoid the $1/f$ noise of the SOT that is present at frequencies below ~1 kHz, an *ac* signal due to backgate modulation was acquired instead of measuring the local *dc* $B_z(\boldsymbol{r})$. We applied a small *ac* excitation to the backgate (Fig. 1a), $V_{bg} = V_{bg}^{dc} + V_{bg}^{ac}\sin(2\pi f t)$, where $f \cong 3$ kHz, and the corresponding $B_z^{ac} = V_{bg}^{ac}\partial B_z/\partial V_{bg}$ was then measured by the SOT using a lock-in amplifier. Another major advantage of this modulation is that it provides a convenient method for direct imaging of the local current density $J(\boldsymbol{r})$. To demonstrate its principle, consider a θ gradient in the $\hat{x}$ direction that gives rise to a narrow strip of current of width Δx, positioned at x_0, and carrying a current density J_y in the $\hat{y}$ direction with a total current $I_y = \Delta x J_y$ (Extended Data Figs. 4a and 4h). The magnetic field $B_z(x)$ generated by the current and measured at height h above it, is described by the Biot Savart law (Extended Data Fig. 4b). For heights $h > \Delta x$ the $B_z(x)$ is essentially governed only by the total current I_y in the strip, independent of Δx. The $B_z(x)$ is an antisymmetric function with a steep slope above the current strip. Its spatial derivative $\partial B_z/\partial x$ has a sharp peak at the strip location (Extended Data Fig. 4c) with a height proportional to I_y and thus can provide a good means for direct imaging of the current density distribution $J_y(x)$ if the latter can be modulated in space in the $\hat{x}$ direction. The backgate voltage V_{bg}^{ac} provides such spatial modulation as follows. In the presence of potential gradients, the QH edge channels flow along equipotential contours (given by equi-θ contours in absence of charge disorder). A small V_{bg}^{ac} thus shifts the location of the channel by $x_0^{ac} = V_{bg}^{ac}\partial x_0/\partial V_{bg}$ in the direction parallel to the gradient and perpendicular to the current flow. So regardless of the gradient direction $\hat{x}$, the measured signal will be given by $B_z^{ac} = -x_o^{ac}\partial B_z/\partial x \propto x_o^{ac} J_y(x)$, thus providing direct imaging of the local current density. Extended Data Figs. 4d-f present a simulation of three counterpropagating current strips demonstrating the B_z^{ac} imaging for this case.

The sharpness of the B_z^{ac} peak is determined by Δx, h, x_0^{ac}, and the SOT diameter. In Fig. 2a, the scanning height above the MATBG is $h = 70$ nm (including hBN) and effective SOT diameter is 220 nm; hence the spatial resolution is essentially determined by the SOT diameter. For these parameters and $x_0^{ac} = 54$ nm rms, Extended Data Fig. 4c shows that a current strip that is narrower than ~150 nm will result in resolution limited B_z^{ac} peak (compare solid and dashed lines).

We now use this numerical procedure to analyze the data in Fig. 2a that presents B_z^{ac} signal along the white dashed line in Fig. 3a, which is aligned along the twist-angle gradient in a region of relatively smooth $\theta(\boldsymbol{r})$ behavior (light-brown region in the top-left corner of Fig. 3b, see also Supplementary Video

1). Extended Data Fig. 4g presents an example of the B_z^{ac} data from Fig. 2a at $V_{bg} = -10.54$ V displaying the B_z^{ac} peak (blue). The data at consecutive V_{bg} values show that the peak position x_0 shifts with V_{bg} at a rate of $\frac{\partial x_0}{\partial V_{bg}} = 1.54$ μm/V, corresponding to a twist-angle gradient $\frac{\partial \theta}{\partial x} = C/\left(\frac{\partial x_0}{\partial V_{bg}}\frac{\partial n_s}{\partial \theta}\right) = 0.0374$ °/μm (where $\frac{\partial n_s}{\partial \theta} = \frac{16}{\sqrt{3}}\frac{\theta}{a^2}$). The data was acquired with $V_{bg}^{ac} = 35$ mV rms, inducing $x_0^{ac} = V_{bg}^{ac}\frac{\partial x_0}{\partial V_{bg}} = 54$ nm rms. The red curve in Extended Data Fig. 4g shows a numerical fit to the data using these experimental parameters and current strip width of $\Delta x = 50$ nm, resulting in $I^T = 1.3$ μA. The good fit shows that the experimental results are consistent with COMSOL simulations in Figs. 4f-i, although the exact value of Δx cannot be determined since the experimental B_z^{ac} peak is resolution limited by the SOT diameter.

The extracted value of $I^T = 1.3$ μA is not sensitive to precise Δx. Since $I^T = \sigma_{yx}\Delta\varepsilon_n/e = \nu\Delta\varepsilon_n e/h$, and $\nu = -12$ in Extended Data Fig. 4g, we attain $\Delta\varepsilon_n = 2.8$ meV comparable to the values derived from band structure calculations (Extended Data Fig. 10a). Using $\Delta x = 50$ nm we attain in-plane electric field in the incompressible region of $E_{\|} = \Delta\varepsilon_n/(e\Delta x) = 56$ kV/m comparable to the simulation values in Fig. 4g.

Topological and nontopological currents in the incompressible and compressible QH strips

Gradients in the twist angle $\nabla\theta$ give rise to gradients in the chemical potential $\nabla\mu$ and to alternating compressible (when μ resides within a LL) and incompressible (μ in the energy gap between LLs) QH strips (Figs. 4f-i). Both regions carry current [42], however, usually only the currents in the incompressible strips, $\boldsymbol{J}^T = \sigma\boldsymbol{E}$, which are of topological nature, are considered, while the nontopological currents in the compressible strips, $\boldsymbol{J}^{NT} = \mu_e\nabla\times|n_e|\hat{z}$, are commonly ignored (here $\mu_e = \epsilon_k/B$ is the magnetic moment of the orbiting electron and ϵ_k is its kinetic energy [43]). The following semiclassical picture is instructive in describing J^T and J^{NT}. Under strong magnetic fields and in the absence of in-plane electric fields, the charge carriers follow cyclotron orbits which can be described semiclassically as an array of circles, resulting in zero average bulk current (Extended Data Fig. 5a). Applying an external in-plane electric field along the x-direction, $E_x = -\partial V/\partial x$, to an incompressible state, causes the circular orbitals to convert into spirals drifting along the y direction, generating a current $J_y^T = \sigma_{yx}E_x$ (Extended Data Fig. 5b). On the other hand, applying the same external electric field to a compressible strip will result in carrier redistribution which screens the in-plane electric field. As a result the drift current vanishes, but at a cost of a non-zero gradient in the carrier density $\partial n_e/dx$ (Extended Data Fig. 5c). Since each orbital carries a magnetic moment $\boldsymbol{\mu}_e = \mu_e\hat{z}$ which gives rise to local magnetization $\boldsymbol{m} = |n_e|\boldsymbol{\mu}_e$, the induced $\partial n_e/\partial x$ causes gradients in $\boldsymbol{m}$, and hence produces equilibrium currents through $\boldsymbol{J}^{NT} = \nabla\times\boldsymbol{m}$ [42]. This accounts for a non-zero $J_y^{NT} = \mu_e\partial|n_e|/\partial x$ (cyan arrows in Extended Data Fig. 5c), which flows in the direction opposite to the topological current J_y^T in Extended Data Fig. 5b. Since a full band does not contribute to current, n_e in the above expression refers only to carriers in a partially filled band. Alternatively, J_y^{NT} can be understood as arising from uncompensated contributions to the current from neighboring orbitals in the presence of a gradient in the orbital density (Extended Data Fig. 5c).

The total current carried by the drifting orbitals in an incompressible strip residing between two compressible regions is given by $I_y^T = \int J_y^T dx = \sigma_{yx}\Delta\varepsilon_n/e$, where $\Delta\varepsilon_n = \varepsilon_{|n|+1} - \varepsilon_{|n|}$ is the LL energy gap between the adjacent compressible states and $\sigma_{yx} = \nu e^2/h$ is QH conductance of the incompressible state (see Fig. 4). For a more extensive description of J^T and J^{NT} see Ref. [9].

Determination of twist angle measurement accuracy and spatial resolution

$\boldsymbol{\theta}$ accuracy. The local twist angle is determined by the local $n_s(\boldsymbol{r})$ through $\theta(\boldsymbol{r}) = a\sqrt{\sqrt{3}n_s(\boldsymbol{r})/8}$. The incompressible I^T current and the corresponding peak in the B_z^{ac} signal appear at specific locations where N LLs in the dispersive bands are exactly fully occupied, corresponding to a density $|n_N| = C\left|V_{bg}^N - V_{bg}^{CNP}\right| = n_s + 4N|B_a|/\phi_0$ for 4-fold degenerate LLs, where V_{bg}^N is the backgate voltage that corresponds to the N^{th} peak. Measuring the N^- and N^+ peaks in the *p* and *n* dispersive bands respectively, allows derivation of $n_s(r) = C\left(\left|V_{bg}^{+N}\right| + \left|V_{bg}^{-N}\right|\right)/2 - 4N|B_a|/\phi_0$ and therefore of $\theta(\boldsymbol{r})$. The absolute angle accuracy is thus determined by the accuracy of C, B_a, and $V_{bg}^{\pm N}$. Determination of C is possible through global transport measurements and more accurately through local measurement of the spacing between any two incompressible peaks $V_{bg}^{N+1} - V_{bg}^N = g|B_a|/(\phi_0 C)$, where g is the degeneracy of the Landau level considered. From this we estimate our overall absolute accuracy of determining n_s to be about $\pm$1%, and thus absolute θ accuracy of $\delta\theta = \pm 0.005°$.

In this study, however, we are particularly interested in the relative accuracy of $\theta(\boldsymbol{r})$ for comparing different locations $\boldsymbol{r}$ and deriving the angle gradients $\nabla\theta$, which is determined essentially only by the measurement precision of $V_{bg}^{\pm N}$. The sharpness of the I^T peaks and the good signal to noise ratio of the B_z^{ac} signal allow high precision measurement of $V_{bg}^{\pm N}$ as demonstrated in Extended Data Fig. 6. In the stationary measurement in Extended Data Fig. 6a (zoom-in of Fig. 1f), V_{bg} was swept with increments $\Delta V_{bg} = 4.7$ mV demonstrating that the V_{bg}^{-3} and V_{bg}^{-4} peak positions can be determined to an accuracy better than $\pm$ one step size ΔV_{bg}, corresponding to $\delta V_{bg}^{-4}/V_{bg}^{-4} \approx 4 \times 10^{-4}$. Since $\theta \propto \sqrt{n_s}$ we have $\delta\theta/\theta \approx 2 \times 10^{-4}$, or relative θ accuracy of $\delta\theta = \pm 0.0002°$. In Supplementary Video 1, that was used to construct the full $\theta(\boldsymbol{r})$ map of device *A* (Fig. 3b), larger increments ΔV_{bg} of 40 mV were used (Extended Data Fig. 6b), corresponding to θ accuracy $\delta\theta = \pm 0.002°$. Supplementary Videos 3, 4 used $\delta V_{bg} = 45$ mV constructing the $\theta(x, y)$ map of device *B* (Fig. 3f) with similar accuracy. Supplementary Videos 3, 4 contain 87 frames of 68×184 = 12,512 pixels each, that were acquired over a total of 42 hours. The V_{bg} trace of each pixel therefore took $t = 12$ seconds to acquire. The $\delta\theta \lesssim \pm 0.002°$ accuracy, normalized by the pixel acquisition time provides the relative θ sensitivity per pixel in the imaging mode is better than $S_\theta^{1/2} = \sqrt{t}\delta\theta = 0.004°/\text{Hz}^{1/2}$.

Spatial resolution of $\boldsymbol{\theta}(\boldsymbol{r})$ mapping. Our electrostatic simulations show that the typical width of the incompressible I^T strips is about 50 nm (Figs. 4f,h) and should be smoothened by the wavefunction width, of the order of magnetic length $l_B = \sqrt{\hbar/eB} \cong 25$ nm. Since the position $\boldsymbol{r}$ of the incompressible strip provides a very accurate determination on the local $n_s(\boldsymbol{r})$ and $\theta(\boldsymbol{r})$, the width of the strip essentially determines the spatial resolution which can be smaller than the SOT diameter. The actual spatial resolution δr is determined by the accuracy δV_{bg} with which the V_{bg} value can be assigned to the I^T peak at a location $\boldsymbol{r}$, $\delta r = \delta V_{bg}\partial r/\partial V_{bg}$, where $\partial r/\partial V_{bg}$ is the change in position of I^T per change in V_{bg}. Since I^T appears at $V_{bg}(\boldsymbol{r}) = (n_s(\boldsymbol{r}) + 4N|B_a|/\phi_0)/C$, the space dependence enters only through $n_s(\boldsymbol{r}) = n_s\big(\theta(\boldsymbol{r})\big)$, therefore $\partial r/\partial V_{bg} = C(\partial\theta/\partial r)^{-1}(\partial n_s/\partial\theta)^{-1}$, where $\partial n_s/\partial\theta = 16\theta/\sqrt{3}a^2$. Using characteristic values $C = 2.5\times10^{11}$ V^{-1} cm^{-2}, $\delta V_{bg} = 45$ mV in the scanning mode, and $\partial\theta/\partial r = 0.05°/\mu$m gives a resolution $\delta r = 50$ nm. Lower $\partial\theta/\partial r$ gradients result in higher δr. In such case, however, since θ varies slowly in space, a lower spatial resolution is required. The estimated δr is comparable to the pixel size in the videos (57 nm in Supplementary Video 1 and 43 nm in Videos 3, 4). We thus conclude that the spatial resolution δr of the attained $\theta(\boldsymbol{r})$ maps is of the order of 4 to 5 moiré supercells (13 nm each).

Local quantum Hall measurement in device *A*

Extended Data Fig. 7 presents the local B_z^{ac} measurement, with SOT parked at a fixed position, along with the global transport R_{xx} measurement in device *A* at $B_a = 1.19$ T. Alternating compressible and incompressible states in the region under the tip lead to a series of peaks in B_z^{ac}, with sharp peaks corresponding to incompressible strips carrying I^T. The sign of the incompressible peaks is determined by the sign of σ_{yx}, with $B_z^{ac} > 0$ (< 0) for electron (hole) doping. In Figs. 1d and 2a the B_z^{ac} signal for *p* doping was multiplied by minus one for clarity. The spacing between adjacent peaks reflects the degeneracy of the LL. The dispersive band (shaded yellow), exhibits a sequence of 4-fold and 8-fold degeneracies. In the flat band we find 4-fold degenerate levels around $n_e = 0$, 2-fold degeneracy near $n_e = \pm n_s/2$, and 1-fold degenerate levels near $n_e = -3n_s/4$ (see Fig. 1d for 1-fold degenerate levels near $n_e = +3n_s/4$). Evaluation of the local n_s allows the extraction of the local twist angle, $\theta = 1.136 \pm 0.005^\circ$ as described below. In contrast to the sharp B_z^{ac} local peaks, oscillations in R_{xx} are hardly visible due to $\theta(\boldsymbol{r})$ disorder and the fact that the MA regions in device *A* do not extend over the entire device area.

Landau level tomography and twist-angle mapping

In order to map the local twist angle, a series of $B_z^{ac}(\boldsymbol{r})$ area scans were performed upon varying V_{bg}. This results in a 3D dataset with two spatial dimensions and one V_{bg} (or equivalently n_e) axis. Each LL energy gap forms a 2D manifold in this 3D space with a peak in B_z^{ac} signal (bright in Extended Data Fig. 8). The manifolds of the lowest LLs in the dispersive bands trace the manifold of the bottom of the dispersive band, $n_s(r)$, and are displaced vertically from it by the degeneracy of the LLs, thus providing the means for mapping the local $n_s(\boldsymbol{r})$ and hence the local $\theta(\boldsymbol{r}) = a\sqrt{\sqrt{3}n_s(\boldsymbol{r})/8}$. The 3D space was mapped with pixel size of ~50 nm and V_{bg} spacing between successive scans, $\Delta V_{bg} \cong 40$ mV, which allows mapping $\theta(\boldsymbol{r})$ with accuracy $\delta\theta = \pm\, 0.001^\circ$ (see Methods).

For device *A*, the tomographic imaging was acquired for the *p* dispersive band for V_{bg} spanning -8.58 V to -11.50 V with $\Delta V_{bg} = 40$ mV (Supplementary Video 1). The spacing between adjacent 4-fold levels at $B_a = 1.22$ T was 0.39 V $\cong 10\Delta V_{bg}$. In this device, the spatial variation of the charge neutrality voltage $V_{bg}^{CNP}(r)$ was found to be very small (Fig. 2a) and therefore $n_s(\boldsymbol{r})$ was derived from the 3D data assuming a constant V_{bg}^{CNP}. Representative slices of the 3D dataset are shown in Extended Data Figs. 8a,b. At $V_{bg} = -8.5$ V, the Fermi level resides in the flat band for all points in space, and at $V_{bg} = -11.5$ V, ε_F is in the dispersive band. As ε_F moves through the bottom of the dispersive band, it crosses four 4-fold degenerate LLs above n_s followed by an 8-fold degenerate LL. The black line in Extended Data Fig. 8a traces the $N = -4$ incompressible I^T peak revealing $\theta(\boldsymbol{r})$ gradients with occasional small jumps in the twist angle. Note that at the jump positions, the intensity of the B_z^{ac} signal is suppressed due to pinning of the LLs at the $\theta(\boldsymbol{r})$ steps, which reduces the amplitude of the spatial *ac* displacement x_0^{ac} and hence the intensity of B_z^{ac} (see Methods).

Note that at any value of V_{bg} several different LLs cross ε_F in the bulk of the sample. Thus despite the fact that fully developed LLs are present locally, no well-defined QH state can be observed globally, explaining of the fact that MATBG magnetotransport commonly shows SdH oscillations without displaying full conductance quantization [1–7]. At high enough field, the QH quantization should be recovered as the LL degeneracy $4B_a/\phi_0$ exceeds the $n_s(\boldsymbol{r})$ variations.

Device *B* exhibited stronger charge inhomogeneity and hence the 3D tomographic imaging was acquired for both *p* and *n* dispersive bands (Supplementary Videos 3 and 4) and $n_s(\boldsymbol{r})$ was derived from the

separation between the corresponding LLs in the two bands as described schematically in Fig. 1f. The tomographic data of both samples is available on [30].

The observation of correlated physics in devices with twist-angle disorder of ~0.1° may be explained by either a tolerance of MA physics to the exact θ or by percolating paths along very specific θ_M. The fact that both of our devices show global MATBG physics including superconductivity, while having only a small overlap in their histograms in Fig. 3i, supports the former. Figure 2a shows, however, that LLs near $n_s/4$ and $n_s/2$ are quite discontinuous and those above $3n_s/4$ appear only at a few locations, indicating the extreme fragility of the correlated states to twist-angle disorder.

Mapping of the charge disorder

Similarly to the mapping of the twist angle disorder through $n_s(\boldsymbol{r}) = C(V_{ns}(\boldsymbol{r}) - V_{-ns}(\boldsymbol{r}))/2$, the tomographic imaging also allows mapping of the charge disorder $\delta n_d(\boldsymbol{r}) = C\big(V_{ns}(\boldsymbol{r}) + V_{-ns}(\boldsymbol{r})\big)/2 - \bar{n}_d$, as presented in Fig. 3h for device *B*. Extended Data Fig. 9 shows the histogram of $\delta n_d(\boldsymbol{r})$ along with a Gaussian fit exhibiting standard deviation $\Delta n_d = 2.59\times10^{10}$ cm^{-2}, which is comparable to high-quality hBN encapsulated monolayer graphene devices [44] and significantly lower than in graphene on SiO_2 [45]. Note that in contrast to hBN encapsulated graphene, MATBG fabrication process is currently incompatible with thermal annealing procedures for disorder reduction. We observe that the charge disorder in device *B* is notably larger than in the MA regions in device *A* (Fig. 2d), which we ascribe to the fact that in contrast to the latter, device *B* did not undergo surface residues cleaning by AFM.

Note that the tomographic method allows mapping of the twist angle and charge disorders only in the MA regions where LLs are present. In device *A*, a significant part of the sample did not show MA physics (Supplementary Videos 1, 2 and Figs. 3a,b) while the regions of MA revealed very low charge disorder with an estimate standard deviation $\Delta n_d \approx 1.3\times10^{10}$ cm^{-2} as attained by several 1D scans like e.g. Figs. 2a,d. We therefore performed tomographic imaging of only the *p* dispersive band which does not allow extracting the full 2D map of $\delta n_d(\boldsymbol{r})$ in device *A*. Neglecting this low level of charge disorder introduces an error in the derived $\theta(\boldsymbol{r})$ map of device *A* of $\delta\theta \lesssim 0.0015°$, which is negligible compared to the span of $\theta(\boldsymbol{r})$ in Fig. 3b.

Band structure calculations and Landau level crossings

The band structure of twisted bilayer graphene can be computed from an effective continuum Hamiltonian, which reads [11,12,46–48]

$$H^{(\xi)} = \begin{pmatrix} H_1^{(\xi)} & U^\dagger \\ U & H_2^{(\xi)} \end{pmatrix},$$

where $H_i^{(\xi)}$ is the valley dependent monolayer graphene Hamiltonian for layer i,

$$H_i^{(\xi)} = -\hbar v_F \left(k - K_i^{(\xi)}\right) \cdot \left(\xi\sigma_x, \sigma_y\right),$$

with Fermi velocity v_F and $\xi = \pm1$, indicating the positive and negative valleys, $K_i^{(\xi)}$ is the k-space location of the respective Dirac points in layer i, and U is the interlayer coupling, which reads [48–51]

$$U = \begin{pmatrix} u & u' \\ u' & u \end{pmatrix} + \begin{pmatrix} u & u'\omega^* \\ u'\omega & u \end{pmatrix} e^{i\xi \boldsymbol{G}_1^M \cdot \boldsymbol{r}} + \begin{pmatrix} u & u'\omega \\ u'\omega^* & u \end{pmatrix} e^{i\xi (\boldsymbol{G}_1^M + \boldsymbol{G}_2^M) \cdot \boldsymbol{r}}.$$

Here, $u = 0.0797$ eV and $u' = 0.0975$ eV [49] are coupling constants that give the strength of the interaction between like ($A \leftrightarrow A, B \leftrightarrow B$) and opposing ($A \leftrightarrow B$) sublattices in the two layers, the

difference of which accounts for out-of-plane corrugation, and $\omega = e^{2\pi i/3}$. The Moiré reciprocal lattice vectors, $G_j^M = a_j^{(1)} - a_j^{(2)}$, are given by the difference between the reciprocal lattice vectors in the upper ($a_j^{(1)}$) and lower ($a_j^{(2)}$) layers.

Magnetic field effects can be included by making the substitution $k \to k + eA/\hbar$ in the effective Hamiltonian. Here, A is the vector potential which is related to the static magnetic field via $B = \nabla \times A$. In general, the band structure in a magnetic field cannot be computed because the addition of a spatially dependent vector potential breaks translational invariance. However, at certain values of the magnetic field – specifically when $(SB/h)/e = p/q$, where p and q are co-prime integers and S is the area of the unit cell – a "magnetic" unit cell can be introduced whereupon it becomes possible to solve the Schrödinger equation using the corresponding "magnetic" Bloch conditions [50]. One is then able to construct a Hamiltonian matrix in the basis of the monolayer graphene Landau levels [51,52]. Although the Landau levels basis is unbounded, one can truncate the Hamiltonian matrix at an energy where the higher energy LLs only weakly affect the low energy spectrum. This cut-off energy must be significantly larger than the interlayer coupling characterized by the coupling constants u and u'. The resulting finite matrix can then be diagonalized. This results in a band structure diagram in terms of p/q, which is directly related to the strength of the magnetic field and indirectly related to the twist angle as the Moiré unit cell area, $S = \sqrt{3}a^2/(8\sin^2(\theta/2))$, is proportional to the twist angle θ. For varying magnetic field or twist angle the bands are computed for each individual parameter value assuming that these values are homogeneous throughout the material.

Level crossings in the band structure are observed as one varies the magnetic field or the twist angle. This is owing to the "Rashba-like" splitting of the dispersive bands. In general, this type of splitting leads to two Landau level series, largely overlapping in energy, which cross as a function of magnetic field (Extended Data Fig. 10a) [53]. Similarly, LL crossings are also observed as a function of θ (Extended Data Fig. 10b) as is the case in the experimental data. This is owing to the evolution of the "Rashba-like" splitting with θ (Extended Data Figs. 10c-e).

Origin of the internal in-plane electric field and numerical electrostatic simulations

The origin of the internal electric field in presence of twist-angle gradients can be understood intuitively as follows. An external in-plane electric field applied to graphene (e.g. by charge disorder in the substrate) exerts a force on the electrons. Since thermal equilibrium conditions require zero net force on the carriers, charge redistribution will occur that will create an opposing electric field, leading to screening of the external field and thus achieving the required zero net force. This is the common situation in metals. In the case of MATBG, the backgate induces a uniform carrier density and thus no in-plane electric field is present initially. However, the twist-angle disorder renders a variable chemical potential $\mu(\boldsymbol{r})$ which exerts an in-plane force on the carriers $\boldsymbol{F}_\parallel = -\nabla\mu$. To attain zero net force in thermal equilibrium, an in-plane electric field $\boldsymbol{E}_\parallel = \nabla\mu/q$ therefore must be generated by carrier redistribution. Thus in contrast to the common charge disorder in which the system tends to screen external electric fields, in the case of twist-angle disorder, counterintuitively, the system spontaneously generates internal electric fields in order to counterbalance the force produced by the variable chemical potential. These internal fields do not generate current at zero magnetic field, however, in finite magnetic field transverse topological and nontopological currents will be induced in the ground state.

For results presented in Fig. 4, COMSOL simulations were used for solving electrostatic equations for the potential V and charge density $\rho = -en_e$ at $B_a = 0$ and in the QH state at $B_a = 1.22$ T. The simulations included a backgate at a constant electric potential V_{bg} and a grounded MATBG in a 3×0.5 μm^2 x-z box,

assuming translation invariance along the y axis, with boundary conditions of $E_\perp = 0$ on the box's external surfaces. An iterative self-consistent solution for $V(x, y, z)$ and ρ was obtained, satisfying the following conditions: (1) The electric potential $V(x, y, z)$ depends on ρ through $\nabla \cdot \boldsymbol{E} = \rho/\varepsilon_r\varepsilon_0$ and $\boldsymbol{E} = -\nabla V$ with given V_{bg}, where ε_r is the relative permittivity (we took $\varepsilon_r = 4$ for hBN) and ε_0 is the vacuum permittivity. (2) ρ depends on V through the integrated density of states $\mathcal{N}_e(\mu; \theta)$, where $\mu(x, y) = -qV(x, y)$ and $q = \pm e$ is the carrier charge (negative sign for $\mu > 0$). The integrated density of states $\mathcal{N}_e(\mu; \theta)$ was calculated for $B = 0$ and $B \neq 0$ as described in Band structure calculations section.

Once $V(x, y, z = 0)$ and $\rho(x, y)$ were found in the plane of the MATBG, the incompressible surface currents were calculated using $\boldsymbol{J}^T = -\sigma\nabla V$, where $\sigma_{xy}(x, y) = -\sigma_{yx}(x, y) = -\nu(x, y)e^2/h$ and $\sigma_{xx} = \sigma_{yy} = 0$ are the components of the conductivity tensor σ.

Measurement parameters

All the measurements were carried out at $T = 300$ mK in out-of-plane applied magnetic field B_a.

Figs. 1b and Extended Data Fig. 2b: Device *B*, $I_{ac} = 10$ nA, $V_{bg} = -15$ V to 15 V.

Fig. 1d: Device *B*, $B_a = 1.08$ T, SOT diameter 250 nm, scan height 40 nm, $V_{bg}^{ac} = 20$ mV rms, $\Delta V_{bg} = 6.25$ mV, acquisition time 6 s per point, total acquisition time 8 hours.

Fig. 1f and Extended Data Figs. 6a and 8: Device *A*, $B_a = 1.19$ T, SOT diameter 220 nm, scan height 100 nm, $V_{bg}^{ac} = 15$ mV rms, $\Delta V_{bg} = 4.7$ mV, acquisition time 6 s per point, total acquisition time 12 hours.

Fig. 2: Device *A*, $B_a = 1.22$ T, SOT diameter 220 nm, scan height 60 nm, $V_{bg}^{ac} = 35$ mV rms, pixel size 26 nm, 160 ms per pixel, total acquisition time 21.4 hours.

Fig. 3a and Supplementary Video 2: Device *A*, $B_a = 1.16$ T, SOT diameter 220 nm, scan height 110 nm, $V_{bg}^{ac} = 80$ mV rms, pixel size 60 nm, 60 ms per pixel, acquisition time 60 minutes per frame.

Supplementary Video 1 and Extended Data Figs. 6b and 8a,b: Device *A*, $B_a = 1.22$ T, SOT diameter 220 nm, scan height 60 nm, $V_{bg}^{ac} = 35$ mV rms, pixel size 57 nm, 60 ms per pixel, acquisition time 30 minutes per frame.

Fig. 3e: Device *B*, $B_a = 1.08$ T, SOT diameter 250 nm, scan height 140 nm, $V_{bg}^{ac} = 60$ mV rms, pixel size 50 nm, 60 ms per pixel, acquisition time 33 minutes.

Supplementary Videos 3, 4 and Extended Data Figs. 8c,d: Device *B*, $B_a = 1.08$ T, SOT diameter 250 nm, scan height 70 nm (M3) and 80 nm (M4), $V_{bg}^{ac} = 60$ mV rms, pixel size 43 nm, 60 ms per pixel, acquisition time 25 minutes per frame.

Extended Data Fig. 2a: Device *A*, $I_{ac} = 10$ nA, $V_{bg} = -17$ V to 17 V. Silicon backgate 50 V.

Extended Data Fig. 3a: Device *A*, $I_{ac} = 5$ nA, $V_{bg} = -6$ V to -3.5 V. Silicon backgate 50 V.

Extended Data Fig. 3b: Device *B*, $I_{ac} = 4$ nA, $V_{bg} = -7$ V to -4 V.

Extended Data Fig. 3c: Device *B*, $I_{ac} = 10$ nA, $V_{bg} = -6.5$ V to -4.7 V, $B_a = 0$ T.

Methods references

33. K. Kim, A. DaSilva, S. Huang, B. Fallahazad, S. Larentis, T. Taniguchi, K. Watanabe, B. J. LeRoy, A. H. MacDonald, and E. Tutuc, ''Tunable moiré bands and strong correlations in small-twist-angle bilayer graphene'', *Proc. Natl. Acad. Sci.* **114**, 3364–3369 (2017).

34. L. Wang, I. Meric, P. Y. Huang, Q. Gao, Y. Gao, H. Tran, T. Taniguchi, K. Watanabe, L. M. Campos, D. A. Muller, J. Guo, P. Kim, J. Hone, K. L. Shepard, and C. R. Dean, ''One-Dimensional Electrical Contact to a Two-Dimensional Material'', *Science* **342**, 614–617 (2013).

35. D. Halbertal, J. Cuppens, M. Ben Shalom, L. Embon, N. Shadmi, Y. Anahory, H. R. Naren, J. Sarkar, A. Uri, Y. Ronen, Y. Myasoedov, L. S. Levitov, E. Joselevich, A. K. Geim, and E. Zeldov, ''Nanoscale thermal imaging of dissipation in quantum systems'', *Nature* **539**, 407–410 (2016).

36. M. E. Huber, P. A. Neil, R. G. Benson, D. A. Burns, A. M. Corey, C. S. Flynn, Y. Kitaygorodskaya, O. Massihzadeh, J. M. Martinis, and G. C. Hilton, ''DC SQUID series array amplifiers with 120 MHz bandwidth'', *IEEE Trans. Appiled Supercond.* **11**, 1251–1256 (2001).

37. A. Finkler, D. Vasyukov, Y. Segev, L. Ne'eman, E. O. Lachman, M. L. Rappaport, Y. Myasoedov, E. Zeldov, and M. E. Huber, ''Scanning superconducting quantum interference device on a tip for magnetic imaging of nanoscale phenomena'', *Rev. Sci. Instrum.* **83**, 073702 (2012).

38. A. Finkler, Y. Segev, Y. Myasoedov, M. L. Rappaport, L. Ne'eman, D. Vasyukov, E. Zeldov, M. E. Huber, J. Martin, and A. Yacoby, ''Self-Aligned Nanoscale SQUID on a Tip'', *Nano Lett.* **10**, 1046–1049 (2010).

39. E. O. Lachman, A. F. Young, A. Richardella, J. Cuppens, H. R. Naren, Y. Anahory, A. Y. Meltzer, A. Kandala, S. Kempinger, Y. Myasoedov, M. E. Huber, N. Samarth, and E. Zeldov, ''Visualization of superparamagnetic dynamics in magnetic topological insulators'', *Sci. Adv.* **1**, e1500740 (2015).

40. D. Halbertal, J. Cuppens, M. Ben Shalom, L. Embon, N. Shadmi, Y. Anahory, H. R. Naren, J. Sarkar, A. Uri, Y. Ronen, Y. Myasoedov, L. S. Levitov, E. Joselevich, A. K. Geim, and E. Zeldov, ''Nanoscale thermal imaging of dissipation in quantum systems'', *Nature* **539**, 407–410 (2016).

41. E. Kleinbaum and G. A. Csáthy, ''Note: A transimpedance amplifier for remotely located quartz tuning forks'', *Rev. Sci. Instrum.* **83**, 126101 (2012).

42. M. R. Geller and G. Vignale, ''Currents in the compressible and incompressible regions of the two-dimensional electron gas'', *Phys. Rev. B* **50**, 11714–11722 (1994).

43. P. Kim, ''Graphene and Relativistic Quantum Physics'', in *Duplantier B., Rivasseau V., Fuchs JN. (eds) Dirac Matter. Progress in Mathematical Physics, vol 71. Birkhäuser, Cham*, 2017, 1–23.

44. C. R. Dean, A. F. Young, I. Meric, C. Lee, L. Wang, S. Sorgenfrei, K. Watanabe, T. Taniguchi, P. Kim, K. L. Shepard, and J. Hone, ''Boron nitride substrates for high-quality graphene electronics'', *Nat. Nanotechnol.* **5**, 722–726 (2010).

45. J. Martin, N. Akerman, G. Ulbricht, T. Lohmann, J. H. Smet, K. von Klitzing, and A. Yacoby, ''Observation of electron–hole puddles in graphene using a scanning single-electron transistor'', *Nat. Phys.* **4**, 144–148 (2008).

46. J. M. B. Lopes dos Santos, N. M. R. Peres, and A. H. Castro Neto, ''Graphene Bilayer with a Twist: Electronic Structure'', *Phys. Rev. Lett.* **99**, 256802 (2007).

47. M. Kindermann and P. N. First, ''Local sublattice-symmetry breaking in rotationally faulted multilayer graphene'', *Phys. Rev. B* **83**, 045425 (2011).

48. M. Koshino and P. Moon, ''Electronic Properties of Incommensurate Atomic Layers'', *J. Phys. Soc. Japan* **84**, 121001 (2015).

49. M. Koshino, N. F. Q. Yuan, T. Koretsune, M. Ochi, K. Kuroki, and L. Fu, ''Maximally Localized Wannier Orbitals and the Extended Hubbard Model for Twisted Bilayer Graphene'', *Phys. Rev. X* **8**, 031087 (2018).

50. D. Xiao, M.-C. Chang, and Q. Niu, ''Berry phase effects on electronic properties'', *Rev. Mod. Phys.* **82**, 1959–2007 (2010).

51. R. Bistritzer and A. H. MacDonald, ''Moiré butterflies in twisted bilayer graphene'', *Phys. Rev. B* **84**, 035440 (2011).

52. P. Moon and M. Koshino, ''Energy spectrum and quantum Hall effect in twisted bilayer graphene'', *Phys. Rev. B* **85**, 195458 (2012).

53. F. Mireles and J. Schliemann, ''Energy spectrum and Landau levels in bilayer graphene with spin–orbit interaction'', *New J. Phys.* **14**, 093026 (2012).

Data availability: The data that support the findings of this study are available from the corresponding authors on reasonable request.

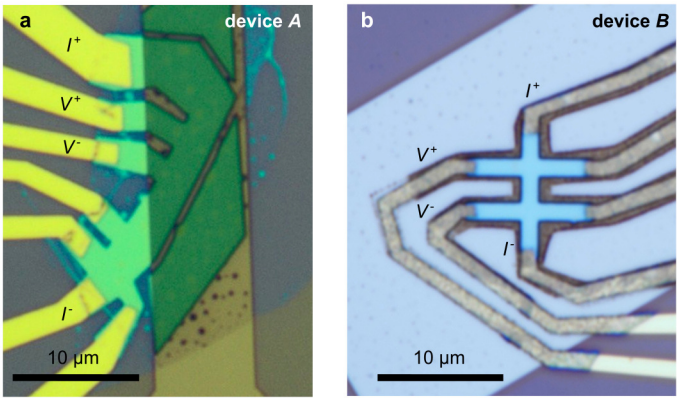

Extended Data Fig. 1. Optical image of MATBG devices. (**a**) Optical image of device *A* showing hBN/MATBG/hBN (green), the underlying PdAu backgate (light brown), and the marked electrodes used for four-probe R_{xx} measurements. (**b**) Optical image of device *B* (cyan) on the PdAu backgate (light blue) with marked electrodes.

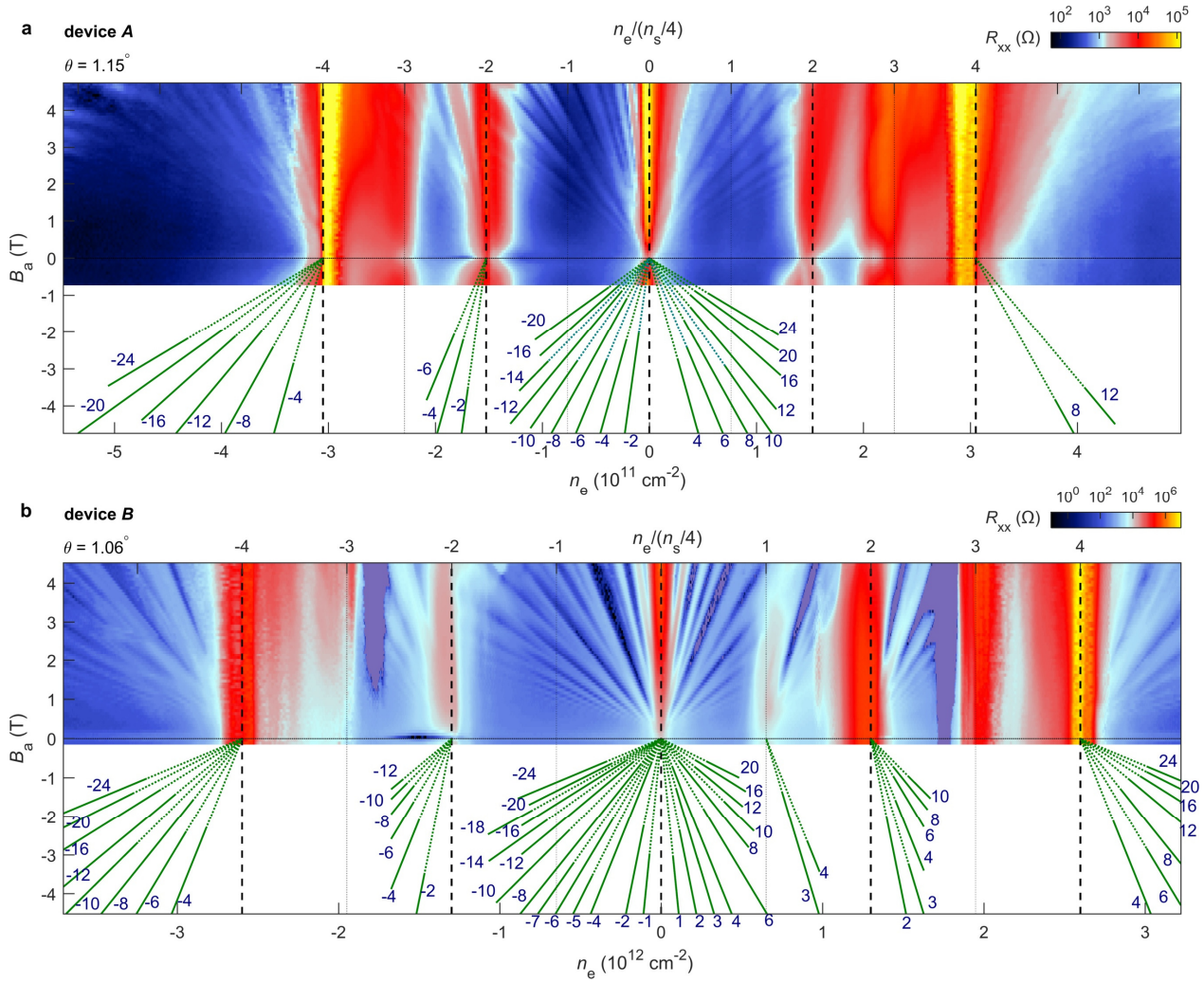

Extended Data Fig. 2. Transport measurements at $T = 300$ mK. (**a**) Four-probe measurement of $R_{xx}(V_{bg})$ vs. B_a in device *A* using excitation current of 10 nA with the corresponding traces of the Landau fan diagram at the bottom. The green solid lines show the segments that can be traced in the data and the dotted lines indicate their extrapolation to the origin. (**b**) Same as (a) for device *B*. The purple color marks the regions where the R_{xx} signal was slightly negative.

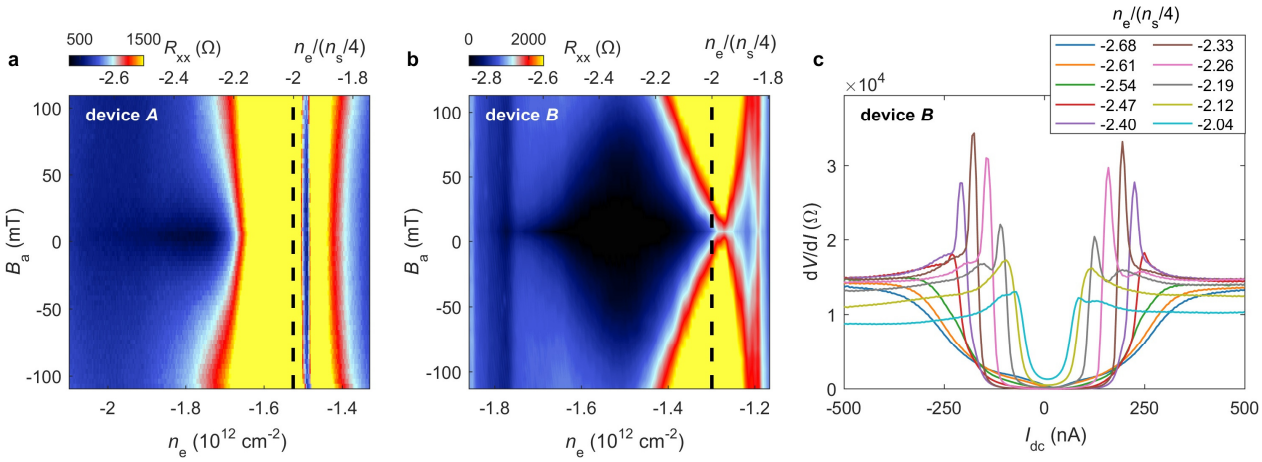

Extended Data Fig. 3. Transport measurements in the superconducting state at $T = 300$ mK. (**a-b**) Color rendering of R_{xx} measured in the vicinity of $-n_s/2$ vs. B_a and n_e at low fields using excitation current of 5 nA rms in device *A* (**a**) and 4 nA rms in device *B* (**b**). A zero resistance superconducting state (black) is observed in device *B*. (**c**) dV/dI vs. I_{dc} characteristics at various carrier concentrations n_e in the superconducting state in device *B* at $B_a = 0$ T using *ac* excitation $I_{ac} = 10$ nA rms.

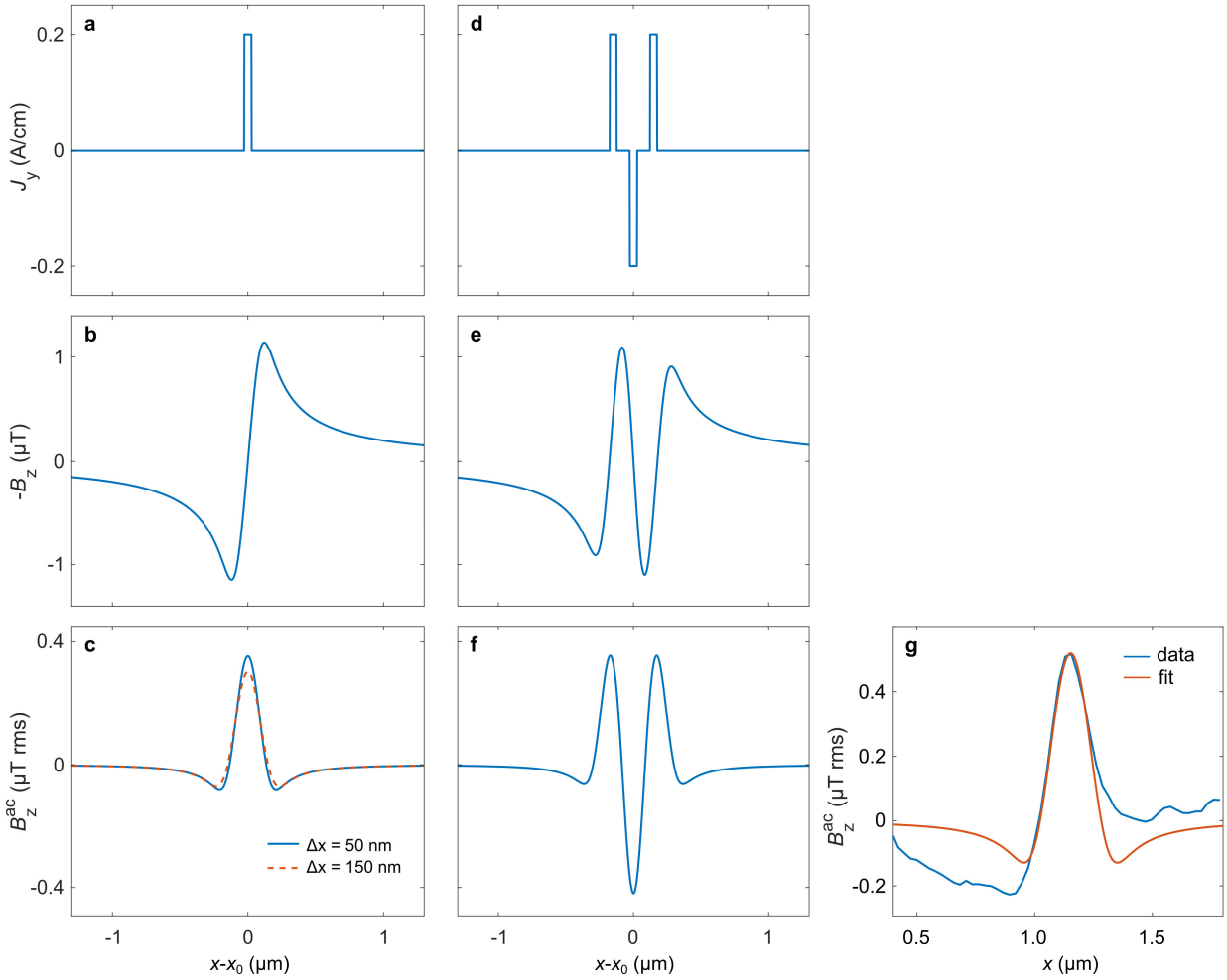

Extended Data Fig. 4. Numerical simulation demonstrating current imaging by measuring B_z^{ac}. (**a**) Current distribution $J_y(x-x_0)$ of a $\Delta x = 50$ nm wide channel carrying $I_y = 1$ μA in the $\hat{y}$ direction. (**b**) Calculated $B_z(x-x_0)$ at a height of 70 nm above the sample convoluted with a 220 nm diameter SOT sensing area. (**c**) Calculated $B_z^{ac}(x-x_0)$ for $x_0^{ac} = 54$ nm rms spatial modulation of the channel position. The dashed profile corresponds to a current strip of width $\Delta x = 150$ nm carrying the same current, showing that the spatial resolution is limited by the SOT diameter. (**d-f**) Same as (a-c) but for three counter-propagating currents spaced 150 nm apart. (**g**) Analysis of the B_z^{ac} peak of an incompressible strip. $B_z^{ac}(x)$ signal (blue) acquired along the line indicated in Fig. 3a for $V_{bg} = -10.54$ V (a single vertical line from Fig. 2a) showing the $\nu = -12$ incompressible peak, along with a numerical fit (red). The fit uses the experimental values of V_{bg}^{ac}, h, and SOT diameter with a single fitting parameter of the total current in the incompressible strip resulting in $I^T = 1.3$ μA. An incompressible strip width $\Delta x =$ 50 nm was used for the fit. The mean value of the $B_z^{ac}(x)$ was subtracted from the data. The asymmetry in $B_z^{ac}(x)$ away from the peak is caused by the presence of counterflowing nontopological currents I^{NT} of lower density in the adjacent compressible strips.

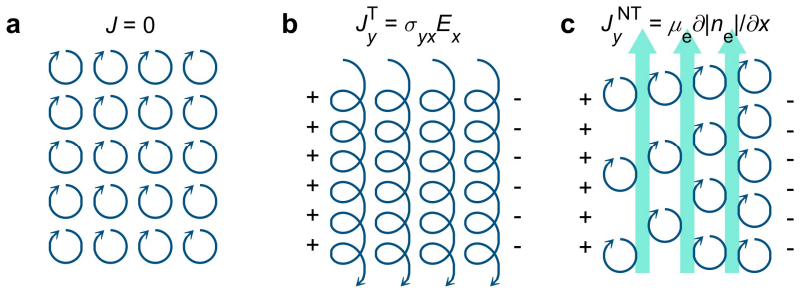

Extended Data Fig. 5. The origin of equilibrium currents in the compressible and incompressible QH states. (**a**) Semiclassical picture of cyclotron orbits of holes with mutually canceling neighboring currents resulting in zero bulk current. (**b**) In the presence of an in-plane electric field E_x (+ and – signs represent external charges) the cyclotron orbits acquire a drift velocity resulting in a non-zero J_y^T in the incompressible state. (**c**) In the compressible regime the external in-plane electric field is screened by establishing a charge density gradient, giving rise to J_y^{NT} flowing in the opposite direction (cyan arrows).

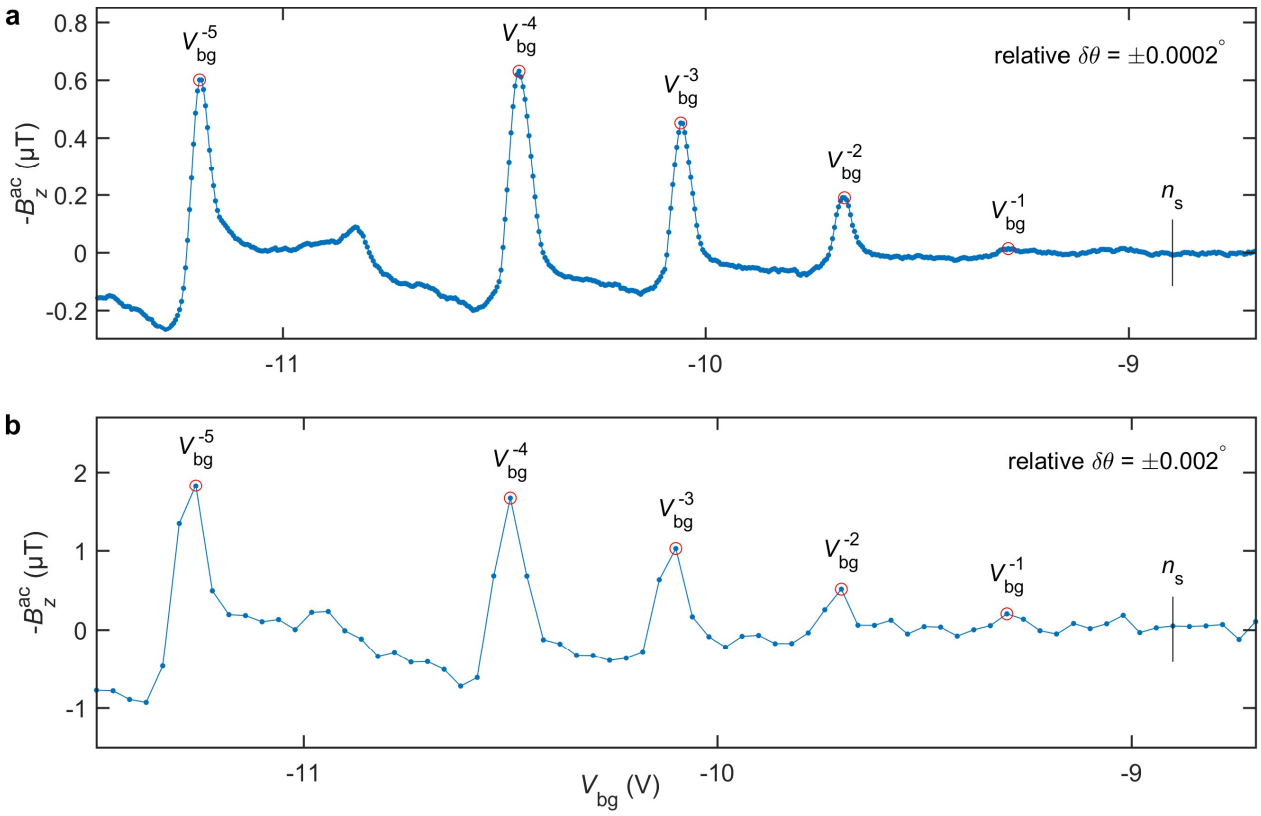

Extended Data Fig. 6. Determination of twist angle measurement accuracy. (**a**) Traces of B_z^{ac} vs. V_{bg} in device *A* (from Fig. 1f) acquired with step size ΔV_{bg} of 4.7 mV and V_{bg}^{ac} = 15 mV rms. The positions of the V_{bg}^{-3} and V_{bg}^{-4} peaks can be determined to an accuracy better than ± one step size ΔV_{bg}, corresponding to relative θ accuracy of $\delta\theta = \pm 0.0002°$. (**b**) Same as (a) taken from Supplementary Video 1 at a pixel position (x, y) = (2.53, 5.9) μm with step size ΔV_{bg} of 40 mV and V_{bg}^{ac} = 35 mV rms resulting in relative θ accuracy of $\delta\theta = \pm 0.001°$ in the imaging mode. The larger B_z^{ac} signal and the broader I^T peaks in (b) compared with (a) is due to higher V_{bg}^{ac} excitation (see Measurement parameters section).

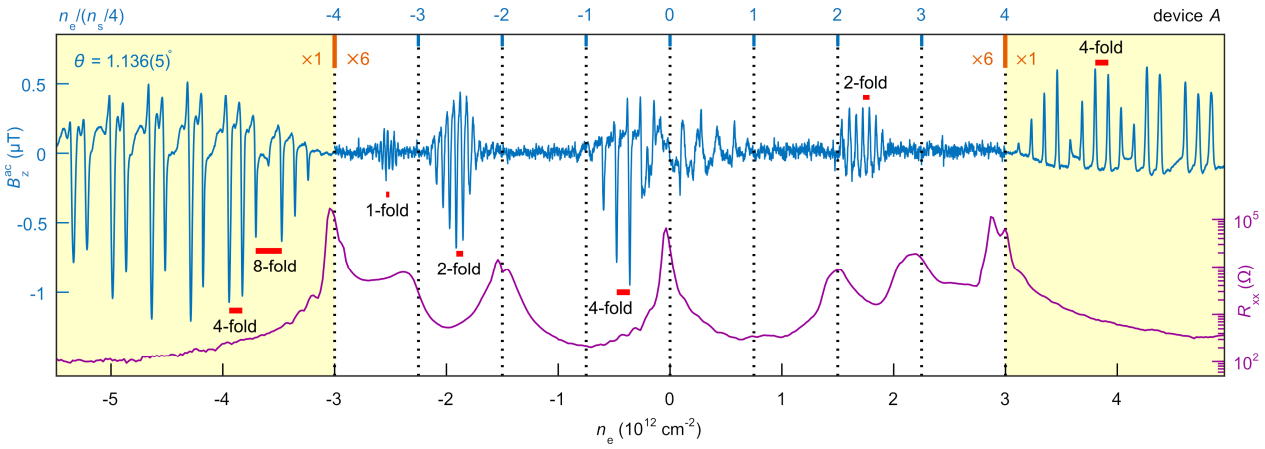

Extended Data Fig. 7. Resolving the local quantum Hall states in flat and dispersive bands in device *A*. Global R_{xx} (right axis) and local B_z^{ac} (left) measured at a point in the bulk of device *A* vs. electron density n_e at B_a = 1.19 T. The sharp B_z^{ac} peaks reflect I^T current in incompressible strips with sign determined by the sign of σ_{yx}, magnitude by the LL energy gap, and separation by the LL degeneracy (red bars). The dispersive bands are shaded in yellow and the signal in flat bands amplified 6 times for clarity.

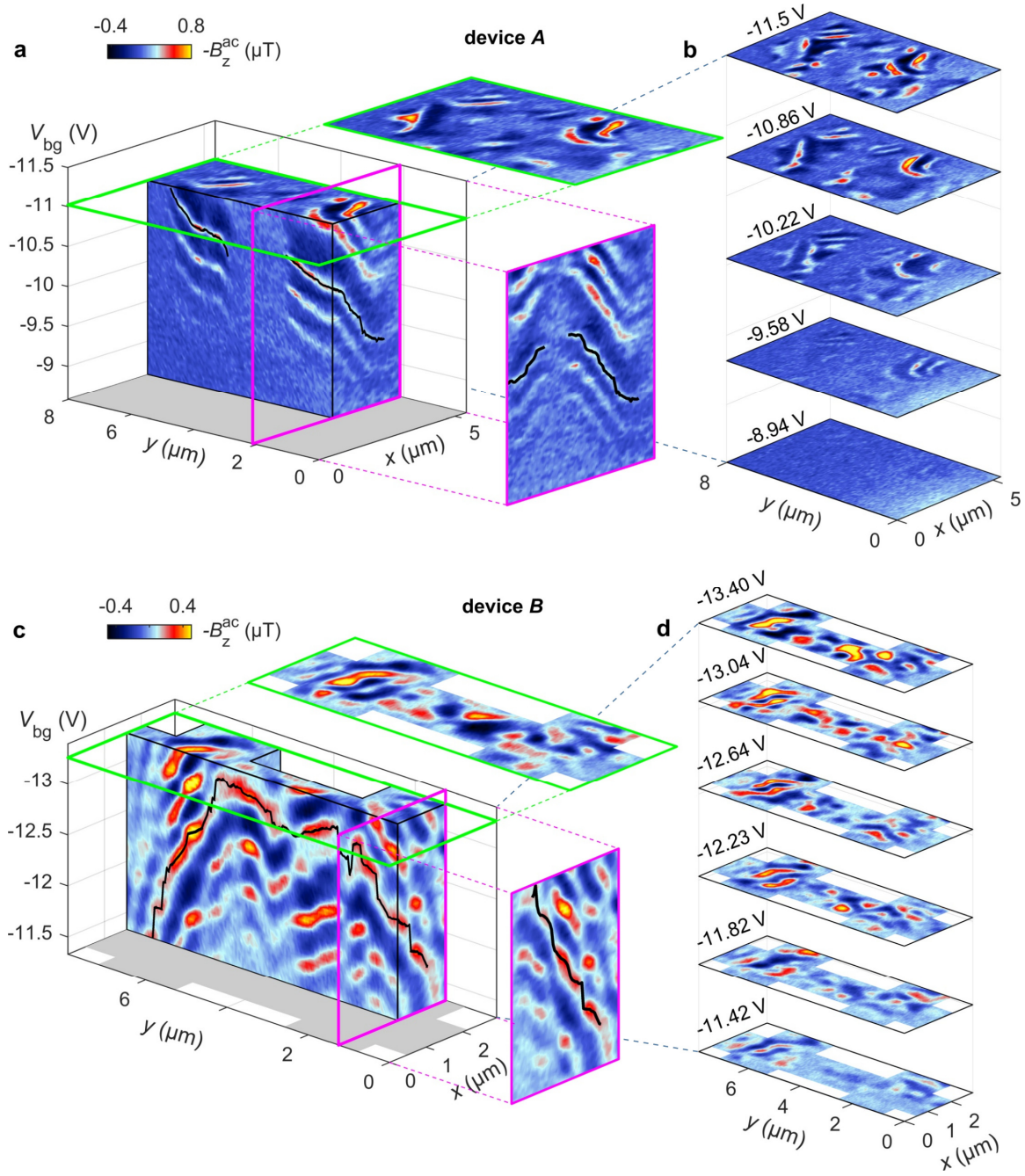

Extended Data Fig. 8. Landau level tomography. (**a**) Slices of the 3D dataset $B_z^{ac}(x, y, V_{bg})$ along various planes for device *A*. The bright signals denote the 2D manifolds tracing the incompressible states. The black lines trace the $N = -4$ incompressible manifold used to determine $n_s(x, y)$ and $\theta(x, y)$. It separates 4-fold degenerate LLs below it from an 8-fold degenerate LL above it (wide dark blue band). The region in the center of the sample showing no LLs corresponds to the grey-blue area in Fig. 3b where no MATBG physics is resolved. (**b**) Representative horizontal slices of the data from Supplementary Video 1 showing the evolution of the LLs with V_{bg}. (**c**) Same as (a) for device *B*. For the range of gate voltages shown, ϵ_F lies in the *p* dispersive band for the entire sample. The black lines show an example of trace of the incompressible manifold lying above an 8-fold degenerate LL. (**d**) Representative horizontal slices of the data from Supplementary Video 3. Interactive interface for tomographic visualization of the data is available on [30].

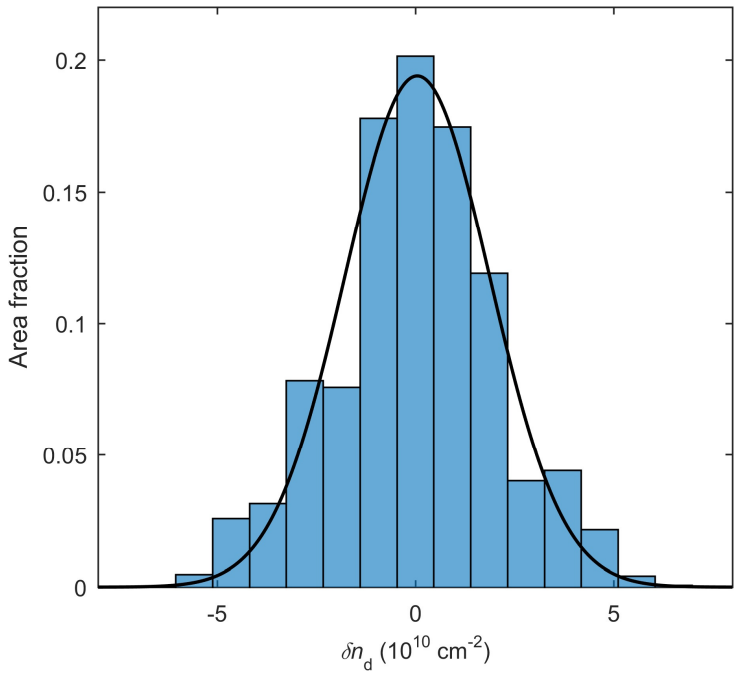

Extended Data Fig. 9. Histogram of the charge disorder in device B. Histogram of $\delta n_d(\boldsymbol{r})$ data from Fig. 3h along with a Gaussian fit (black) with standard deviation of $\Delta n_d = 2.59\times10^{10}$ cm^{-2}.

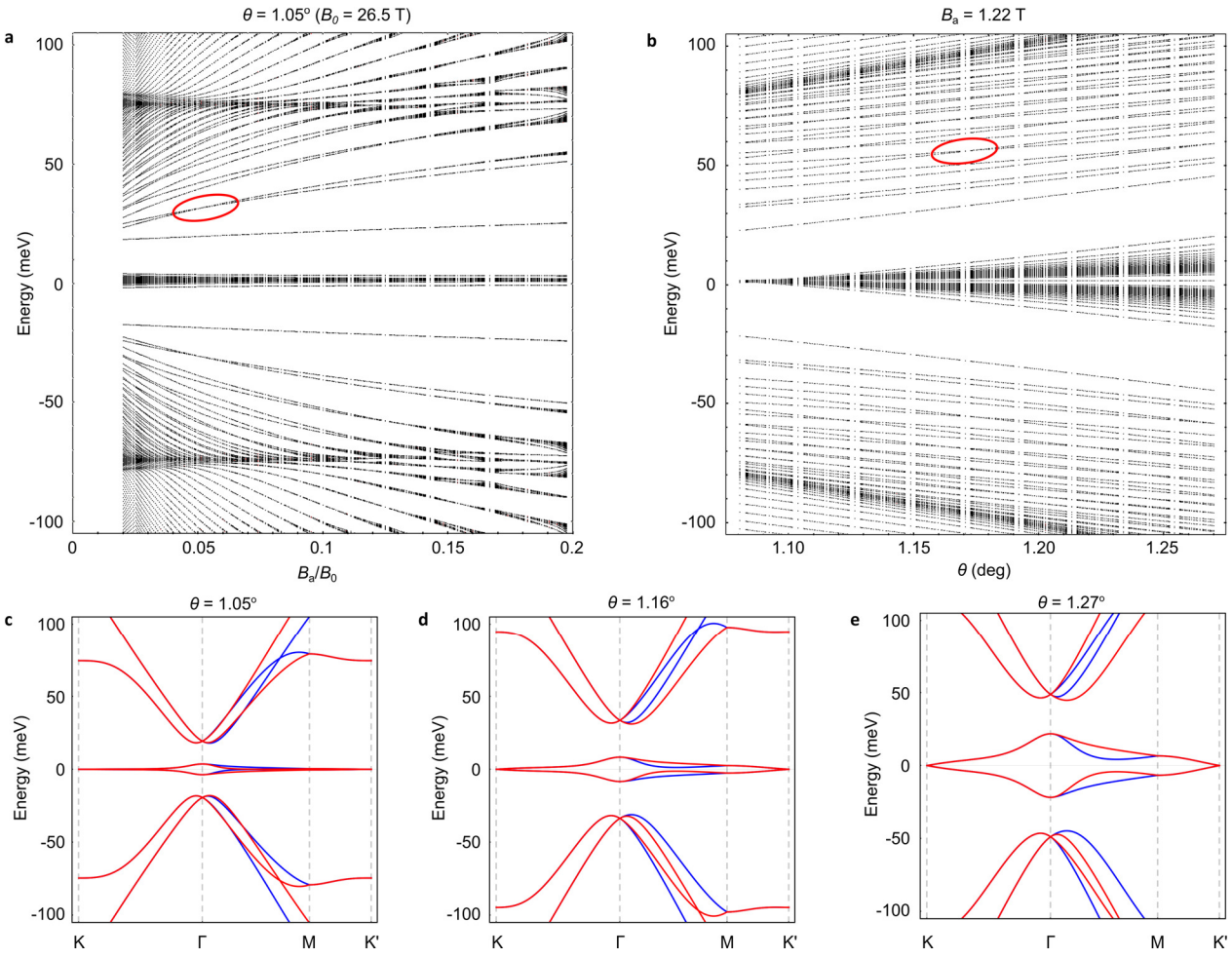

Extended Data Fig. 10. Dispersive bands Landau level crossings. (**a**) Numerically calculated LL energies as a function of magnetic field for a fixed $\theta = 1.05°$. An example of level crossing is highlighted in red. (**b**) Numerically calculated LL energies as a function of θ for a fixed $B_a = 1.22$ T. An example of a level crossing is highlighted in red. (**c**-**e**) The $B_a = 0$ band structure of bilayer graphene for $\theta = 1.05°$ (**c**), 1.16° (**c**), and 1.27° (**c**). The blue and red lines indicate the bands that arise from the positive and negative valleys, respectively.